Optimal methods of WO_3 compositing on SnO_2 surface for highly sensitive semiconductor gas sensors

REN, TAO
Major of Science and Engineering of Materials and Devices, Department of Interdisciplinary Engineering Sciences, Interdisciplinary Graduate School of Engineering Sciences, Kyushu University

修士論文

Optimal methods of WO_3 compositing on SnO_2 surface for highly sensitive semiconductor gas sensors

九州大学大学院総合理工学府総合理工学専攻

材料理工学メジャー

機能材料物性学分野

修士課程２年　任涛

指導教員　

受理日　2023 年 2 月 10 日

Contents

1. Introduction

1.1 Introduction

In the middle of the 19th century, Japan reached the peak of rapid economic growth, and household liquefied petroleum gas became popular. However, many accidents caused by gas leakage and carbon monoxide poisoning have become social problems [1]. Therefore, the development of gas sensors for monitoring the atmospheric environment has been promoted and played an important part of many different types of applications [2-4]. Among them, a metal-oxide-semiconductor (MOS)-based sensor, also known as a chemical resistive gas sensor, has played an important role and has been applied in various applications [5-7]. At the early 1960s, Seyama demonstrated the feasibility of gas sensing using simple electrical devices with a ZnO thin film as the sensing layer [8]. And about the same time, Taguchi fabricated and patented the first chemo-resistive gas sensor device for practical applications using tin dioxide (SnO_2) as the sensitive material [9]. In 1968, Figaro Engineering Co., Ltd. released the first semiconductor-type flammable gas sensor as a commercial product [10]. Following Seyama's work, Shaver [11] detailed the enhancements possible with oxide semiconductors altered by noble metal additions (e.g. Pt, Pd, Rh), leading to enhanced sensitivity and selectivity in semiconductor sensing devices and increased research on new sensing material formulations.

Many gas sensors in practical use today are based on metal oxides, in fact, after studying many metal oxides, it was found that tin dioxide (SnO_2) has many favorable properties and is the main material used. Tin dioxide is characterized by low cost, high sensitivity to low gas concentrations, and good long-term stability, making it useful as a gas sensor material. Many studies have been reported on the addition of precious metals, control of the microstructure of the material, adsorption of gases on the sensor surface, and response mechanisms to improve sensor performance, such as increasing the sensitivity of semiconductor gas sensors, improving selectivity, and suppressing the degradation of sensor response due to water vapor. Recently, clinical diagnosis by detecting biomarkers in exhaled breath both quantitatively and qualitatively has garnered much attention for early, non-invasive identification of various diseases. [12-17]. Human breath contains several volatile organic compounds (VOCs) that represent healthy body conditions. In a healthy person, these VOCs are usually present at levels below ppm or even lower, and their elevated levels can be intuitively correlated with unhealthy, infected or injured body conditions [18-20]. If such sensors can be made smaller, more energy-efficient and can selectively detect gases, they are expected to find applications in mobile products such as smartphones and home medical devices, as well as in multi-sensors that integrate gas sensors to detect various gases.

In this chapter, regarding SnO_2-based semiconductor gas sensors, the conventional SnO_2 semiconductor gas sensor detection mechanisms and the design guidelines for improving the performance of SnO_2 gas sensors based on them are described. Finally, the purpose and outline of this research are described.

1.2 Metal Oxide Semiconductor Gas Sensors

1.2.1 Characteristics and types of semiconductor gas sensors

Semiconductor gas sensors are sensors that use oxide semiconductors to detect gases, utilizing the change in electrical resistance of the semiconductor when the test gas comes into contact with the oxide semiconductor. Metal oxides, with their broad range of structural, physical, and chemical properties and functions, are among the most prevalent, diverse, and possibly extensive classes of materials, including commonly used binary oxides such as SnO_2, ZnO, TiO_2, etc. Additionally, practical gas sensors also utilize ternary and more complex oxides [4]. The change in electrical resistance value is related to complex phenomena on the surface of the semiconductor, such as adsorption of oxygen and the test gas that occurs on the semiconductor surface, and reactions between adsorbents. There are two types of semiconductor gas sensors: one in which the interaction with gas changes the electrical resistance (surface control type) and the other in which the defect structure change due to the reaction between bulk and gas changes the electrical resistance (bulk control type). Table.1.1 shows the classification of electrical resistance type semiconductor gas sensors.

Table.1.1 Classification of electrical resistance type semiconductor gas sensors [21].

Type	**Physical characteristics**	**Materials**	**Operating Temperature**	**Typical target gas**
surface control type	Electrical conductivity	SnO_2, ZnO	Room temperature-450°C	Flammable gas
	Threshold voltage (Transistor)	Pd gate MOSFET	150°C	H_2, H_2S
	Rectification characteristics (diode)	Pd/CdS, Pd/TiO_2	Room temperature-200°C	H_2, CO, Ethanol
	Surface potential	Ag_2O	Room temperature	Mercaptan
bulk control type	Electrical conductivity	$La_{1-x}Sr_xCoO_3$, γ-Fe_2O_3	300°C-450°C	Ethanol, Flammable gas
		TiO_2, CoO-MgO, SnO_2	700°C or more	O_2

The surface control type uses changes in surface conductivity and work function due to gas adsorption, etc. The use of conductivity change in this type was reported by Seiyama et al. [8]. Surface control type semiconductor gas sensors typically require heating above 300°C because gas adsorption and desorption rates on semiconductor surfaces and surface reaction rates are very mild at low temperatures near room

temperature. Therefore, semiconductor materials must be physically and chemically stable at high temperatures and in oxidizing and reducing atmospheres. Metal oxides are the only ones that can meet these requirements. In terms of gas adsorption, n-type semiconductors have less adsorption of electron-absorbing gases such as O_2 than p-type semiconductors. In addition, when considering the resistance aspect, the rate of electron resistance drop for n-type semiconductors is relatively greater than the rate of increase in resistance for p-type semiconductors in atmospheres with electron-abandoning gases such as H_2 and CO. Therefore, semiconductor gas sensors are expected to show good sensitivity, with a large variation in the resistance of n-type semiconductors to combustible gases [22]. The SnO_2 gas sensor used in this study is classified as a surface control type.

The crystal structure of SnO_2 is tetragonal rutile crystal structure. SnO_2 has a density of 6.995 g/cm^3 and is a wide bandgap (3.6 eV) semiconductor with interesting electrical properties [23]. SnO_2 is an n-type semiconductor with a co-ordination number of 6 for Sn^{4+} and an oxygen vacancy as the donor. In particular, SnO_2 is stable in redox atmospheres with high surface activity, and due to its high sensitivity to different gas species, SnO_2-based sensors can detect low concentrations of gas species and are therefore excellent as sensor materials, but unfortunately it suffers from a lack of selectivity. However, strategies dedicated to improve the performance of SnO_2-based devices have been extensively investigated [24]. Therefore, this section describes the detection principles and performance improvements of SnO_2 semiconductor gas sensors.

1.2.2 Gas sensing mechanism

The semiconductor gas sensors detect gases by measuring the change in electrical resistance in air and the gas to be measured. Air is a mixture of two gases, N_2 and O_2 in a ratio of 79%:21%. N_2 is an inert gas and only O_2 affects the resistance. When gases with large electron affinity such as O_2 and NO_2 approach the SnO_2 surface, they lose kinetic energy due to physical adsorption on the particle surface. As shown in Fig.1.1(a), molecules adsorbed on the particle surface are thermally dissociated and chemisorbed on the adsorption site. In other words, a new energy level is created between the Fermi level and the valence band of the semiconductor for the existence of electrons. Thus, charge redistribution in the semiconductor occurs, and electrons in the conduction band of the semiconductor are transferred to the lower energy level of the adsorbed molecule. Since the electrons are trapped by the adsorbed oxygen, the adsorbed molecules become negatively charged and the surface charge density of the semiconductor decreases. When gas adsorption reaches equilibrium, the Fermi level near the semiconductor surface coincides with the electron level of the adsorbed molecules, as shown in Fig.1.1(b), and no electron transfer occurs. This electron depletion layer is formed from the surface to the interior of the particle. When the particles are in this low charge density state, the electrical resistance of SnO_2 is very high.

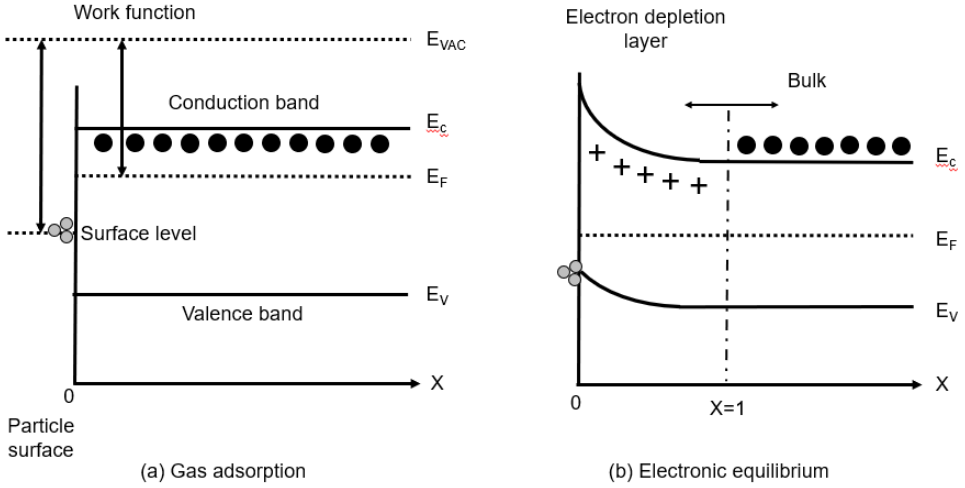

Fig.1.1 Band model of gas adsorption in n-type semiconductors [25].

Next, figure 1.2 shows the gas detection mechanism associated with the adsorption reaction when combustible gas is introduced. In a dry atmosphere, oxygen in the air is negatively charged and adsorbed on the particle surface, causing an electron depletion layer to spread to the interior of the particle, resulting in a high electrical resistance value. In this case, the adsorbed oxygen forms O^- or O^{2-} as shown in the following equation.

$$O_2 + 2e^- \rightarrow 2O_{ad}^- \quad \text{(R1.1)}$$

$$O_2 + 4e^- \rightarrow 2O_{ad}^{2-} \quad \text{(1.2)}$$

Here, when a target gas such as H_2, which is a combustible gas, approaches the particle surface, a combustion reaction occurs with the adsorbed oxygen. At this time, a reaction like the following formula is caused.

$$H_2 + O_{ad}^- \rightarrow H_2O + e^- \quad \text{(1.3)}$$

$$H_2 + O_{ad}^{2-} \rightarrow H_2O + 2e^- \quad \text{(1.4)}$$

As shown in the above equation, H_2 reacts with adsorbed oxygen (O^-, O^{2-}) on the surface of sensing layer at an appropriate operating temperature to form H_2O. The negatively charged adsorbed oxygen on the particle surface is desorbed by reacting with the surface of the target gas, and the captured electrons are returned to the SnO_2 particles. As a result, the surface charge density of the SnO_2 particles increases, leading to a decrease in resistance. In other words, the reaction between H_2 and the negatively charged adsorbed oxygen reduces the amount of negatively charged adsorbed oxygen on the surface of the SnO_2 particles, the surface charge density of the SnO_2 particles increases, and the resistance of the SnO_2 decreases. This change in resistance enables gas detection. Here, the sensor sensitivity S of n-type semiconductors for combustible gases is expressed as the ratio of the resistance R_a in air to the resistance R_g in the target gas to be measured ($S=R_a/R_g$).

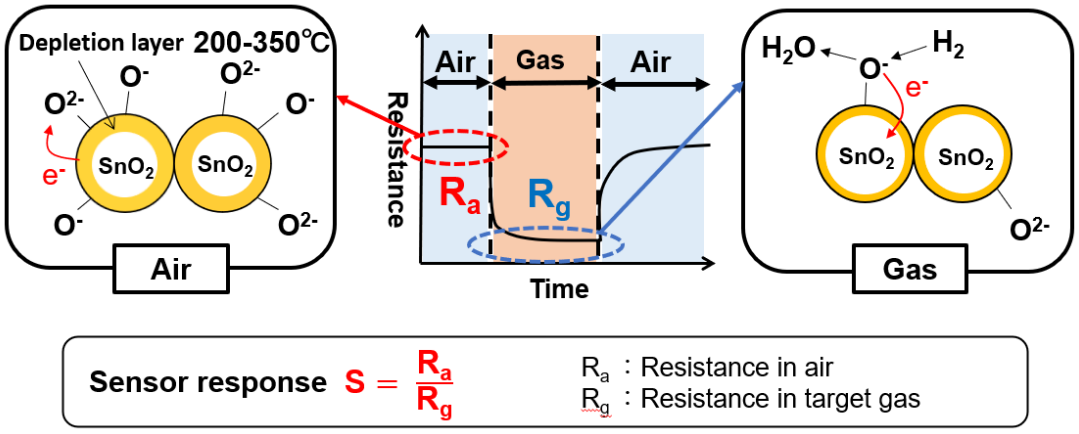

Fig.1.2 Gas detection model of SnO_2 semiconductor gas sensor.

1.2.3 Adsorption on SnO_2 surfaces

(a) O_2 adsorption

Oxygen adsorption is considered to be an important factor in determining sensor characteristics, and numerous studies on oxygen adsorption have been reported. Figure 1.3 shows the results of temperature desorption measurement (TPD) of SnO_2 to oxygen [26]. Oxygen has been reported to adsorb as O_2, O^{2-}, O^-, O^{2-} on the surface of oxides such as SnO_2. This has been confirmed using electrical conductivity measurements and ESR measurements [27]. Temperature programmed desorption (TPD) chromatograms of oxygen displayed the formation of four types of oxygen species on SnO_2 which were desorbed around 80°C (α1), 150°C (α2), 560°C (β), and above 600°C (γ), respectively. Peaks $_1$, $_2$, and are the peaks obtained by elimination of O_2, and are reported to be O_2, O_2^-, O^-, or O^{2-}, respectively. Here, O_2 does not contribute to the change in electrical resistance because it is physical adsorbed and no electron transfer occurs between O_2 and SnO_2. The electron configuration of O^{2-} is energetically more stable than that of O_2 because one electron enters the antibonding orbital of O_2; O^{2-} is readily formed in the presence of an electron donor by trapping an electron from the adsorbed symmetry at low temperature. However, it can be confirmed that desorption of O^{2-} occurs below 250ºC, suggesting that O^{2-} is not stable in the working temperature range of the sensor. Even if O_2 on the surface of SnO_2 particles rises to the temperature at which it dissociates, it is considered that it can exist stably by forming O^- and O^{2-} as electron donation occurs. The γ peak represents the lattice oxygen of SnO_2. In other words, lattice oxygen is released in the temperature range above 600ºC, which is thought to cause the SnO_2 particle surface to be in a reduced state. From these results, it can be considered that O^- or O^{2-} among the oxygen adsorbed species affects the electrical properties of the SnO_2 gas sensor.

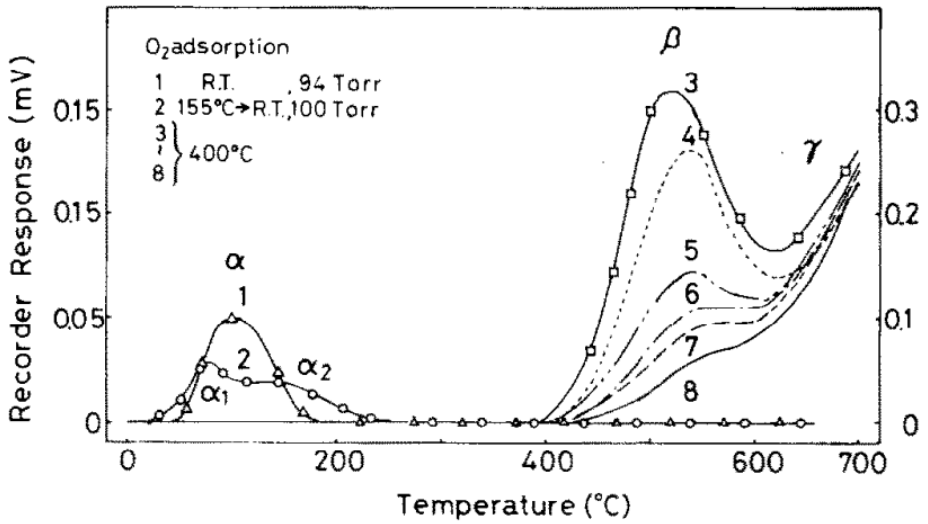

Fig.1.3 The results of temperature desorption measurement of SnO_2 to oxygen [26].

(b) H_2O adsorption

So far, gas detection characteristics in dry atmospheres have been described, but water vapor is present in the atmosphere where the sensors are used. It is necessary to describe the effect of water vapor on the response of gas sensors. Figure 1.5 shows the results of the TPD and conductivity measurement of water vapor using SnO_2. After adsorption by from 600°C to room temperature, two large desorption peaks, and , appeared around 100°C and 400°C, respectively. The conductivity measurement shows that the peak around 400°C affects the conductivity of SnO_2 conductivity. Thornton et al. [28] also analyzed the water vapor adsorbed species using IR spectroscopy. From the measurement results, it was confirmed that molecular adsorption desorbed at 150°C, and desorption of surface hydroxyl groups occurred in the temperature range of 250°C to 500°C. Therefore, it is considered that the adsorption of hydroxyl groups on the SnO_2 surface inhibits the negative charge adsorption of O_2, resulting in a decrease in the electrical resistance of SnO_2.

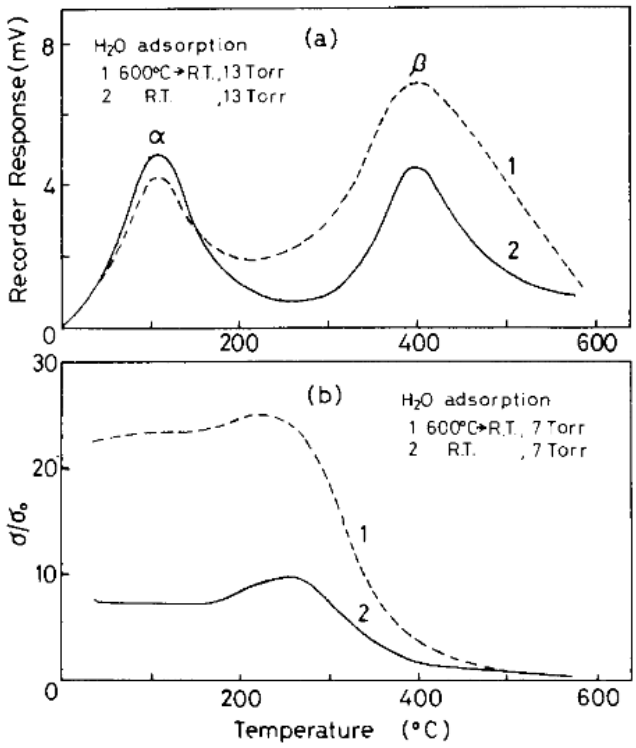

Fig 1.4 TPD measurement results and conductivity change of SnO_2 to water [26].

1.3 Key Factors of Oxide Semiconductor Gas Sensor

Semiconductor gas sensors are used in various gas atmospheres, and research is being conducted to improve their performance, such as improving sensor sensitivity for detecting low concentrations and improving gas selectivity. This section describes (1) the sensitizing effect of the additive (receptor function), (2) the transducer function, and (3) the utility factor of the sensor film by controlling gas diffusion, which are important factors for improving the performance of the semiconductor gas sensor.

1.3.1 Receptor function

The sensitizing effect of low-temperature actuation can be obtained by loading receptors such as noble metals and metal oxides. Figure 1.5 shows the relationship between the sensitivity of SnO_2 sensors loaded with Pt, Pd, and Ag, respectively, to each target gas and the operating temperature [29,30]. From the figure, the sensitivity of the SnO_2-based sensor is significantly increased compared to the neat SnO_2 sensor. Also, it can be seen that the operating temperature showing the maximum sensitivity is shifted to the low temperature side.

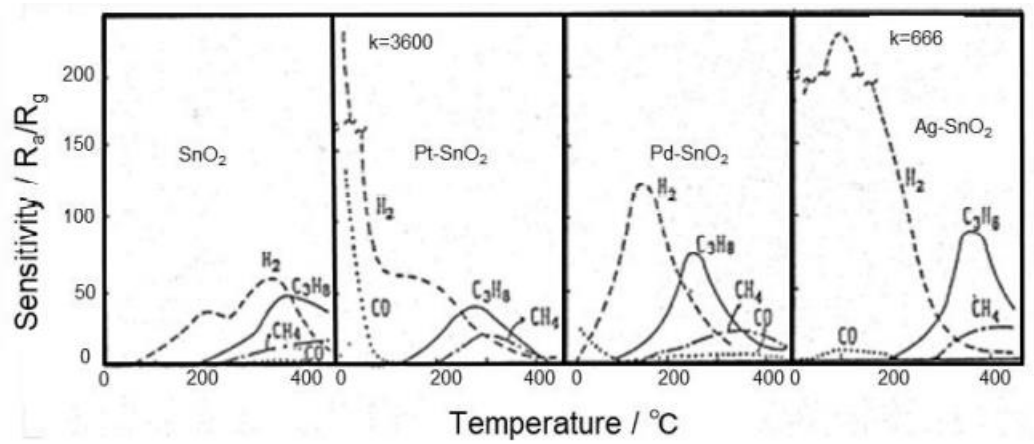

Fig.1.5 Relationship between sensor sensitivity of SnO_2-based gas sensors to various gases and temperature [30].

Figure 1.6 shows the relationship between the temperature at which the conversion reaches 50% (T_{50}) and the temperature at which the maximum sensitivity is observed (T_M) in the combustion reaction experiments of H_2 and C_3H_8 using receptor-loaded SnO_2 as a catalyst. This sensitizing effect is related to the high activity against combustible gases. For target gases, the temperature (T_M) is lowered by the receptor loading as a result of the relationship between the temperature at which the sensor sensitivity is at its maximum and the oxidation temperature. This indicates that oxidative activity is related to the temperature at which sensor sensitivity is maximized. This suggests that the gas detection mechanism is not only simply gas adsorption, but also contact oxidation with the target gas. Therefore, the maximum value of gas sensitivity varies depending on the test gas. In the case of H_2, the sensitivity of H_2 is significantly improved when any of the receptors are loaded.

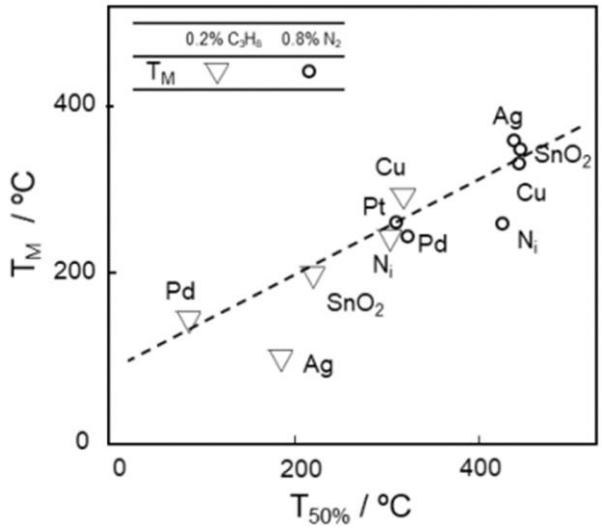

Fig.1.6 The relationship between the temperature (T_{50}) at which the oxidation of H_2 and C_3H_8 reaches 50% addition in SnO_2-based materials and the temperature of maximum gas sensitivity (T_M).

Figure 1.7 shows a model of sensitization by receptors. Such sensitization effects are broadly understood to be mainly (a) chemical interaction and (b) electronic interaction. First, the mechanism of the chemical interaction is that the target gas dissociates at the receptor and spills over to the surface of the oxide semiconductor to react with the adsorbed oxygen. When noble metals such as Pt are loaded, sensitization can be achieved through gas adsorption on the surface of noble metals, activation of gas molecules by additives, overflow of active molecules and reaction with adsorbed oxygen. This kind of sensitization is called chemical sensitization, and it is considered that chemical sensitization is particularly effective when intermediate gases are easily produced in the oxidation process. In addition, sensitization by acid/base modification can be considered as chemical sensitization.

On the other hand, electronic interaction works by changing the electronic bond between the receptor and the oxide semiconductor. For example, Pd is thought to exist as PdO (p-type) in the operating temperature range of the sensor, and in reducing atmospheres such as H_2 or CO, is reduced to exist as the noble metal Pd. Therefore, a p-n junction is formed between PdO (p-type) and SnO_2 (n-type) in air, and PdO acts as a strong electron acceptor, greatly reducing the charge density on the SnO_2 surface and forming a deep depletion layer. Moreover, as PdO exists in the reducing gas in the state of noble metal Pd, the p-n junction disappears and does not function as an electron acceptor, leading to a significant decrease in resistance. In other words, by using Pd as an receptor, high sensor sensitivity can be obtained. This is electronic sensitization. Papers applying this principle have been widely reported [31,32].

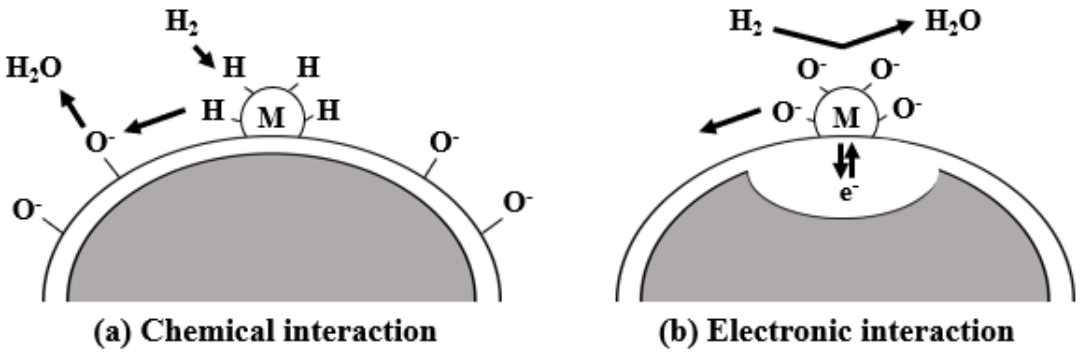

Fig.1.7 A model of sensitization by receptors.

1.3.2 Transducer function

The oxides are physically in contact between fine particles at grain boundaries or by a neck that is thinner than the grain size. The resistance in oxide semiconductor gas sensors is dominated by the resistance at the neck or grain boundaries. The effect of grain size (D) on gas sensitivity using a mixed coupling of these two forms of sensors reported by Xu et al. [34]. Figure 1.8 shows the relationship between sensor electrical resistance and sensor sensitivity and particle size. As the D decreases, the resistance in air (R_a) remains constant up to a critical value (2L), but increases rapidly as it becomes

less than 2L. This phenomenon is similar for the resistance (R_g) in the test gas (800 ppm H_2), indicating that the gas sensitivity (R_a/R_g) increases below 2L. In the case of SnO_2, the thickness of the space charge layer is assumed to be about 3 nm at 300°C, on the other hand, the crystallite size of SnO_2 particles (D) in conventional sensor elements is usually in the order of a few tens nanometer [35]. This is because in the region where D>>2L, the resistance value of the grain boundary contact part to the crystal surface increases and the grain boundary mainly controls the resistance of the device. On the other hand, in the region where D<2L, the space charge layer spreads over the whole particle and the resistance of the particle itself becomes overwhelmingly dominant at the grain boundaries (grain control). As a result, the element resistance in the particle control region increases rapidly in air and target gas, leading to an increase in gas sensitivity. In other words, particle size control of the sensor material plays an important role in improving gas sensitivity.

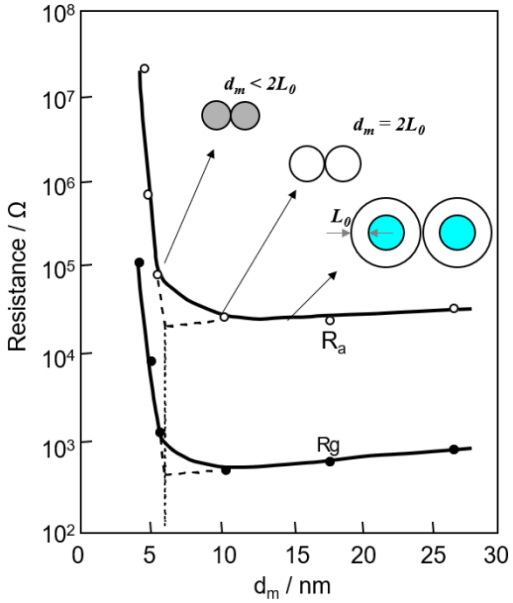

Fig.1.8 Relationship between sensor electrical resistance and sensor sensitivity and particle size.

These explanations suggest that the conductivity occurs when electrons cross the Schottky barrier at the grain boundaries. However, Yamazoe et al.[36-39] reported that grain boundary conductivity can be interpreted as tunneling conduction and that surface charge density affects conductivity. The occurrence of tunnel conduction means that there is an electric charge on the surface of the particle. Thus, a theoretical explanation is given for the adsorption and reaction of charges and gases present on the surface.
It is well known that the resistance value (R) of a semiconductor gas sensor depends on the partial pressure (P) of the test gas, and the resistance value can be expressed by the following equation.

$$R = aP^n \; or \; \log R = a' + n \log P \tag{1.5}$$

Here, a, a' and n are constants, and the power index n is peculiar to the type of the target gas. In the case of SnO_2, n is 1/2 for surface O_2 adsorption -1/2 for surface H_2 adsorption.

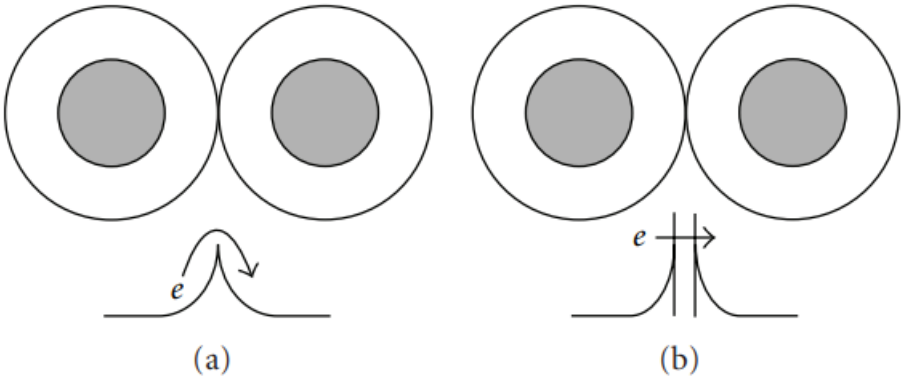

Fig. 1.9 Electrical conduction models [33]
(a) Schottky model (b) Tunnel conduction model

Figure 1.10 shows the change in surface potential as the oxygen partial pressure changes relative to the particle when the microcrystal diameter decreases. Take an example of a crystallite diameter equal to 2a. When the oxygen partial pressure is 0, it is in a flat band state regardless of the crystallite diameter. As the partial pressure of oxygen increases (P_{O2}(I)), the surface charge density decreases with oxygen adsorption, and an electron depletion layer forms from the surface of the grain to the interior. As the oxygen partial pressure increases further (P_{O2}(II)), the electron depletion layer deepens and spreads throughout the crystal. At this point, it can be said that the source of electrons is inside the crystal, and the depletion layer diffuses throughout the crystal after providing electrons by lowering the Fermi energy level. On the other hand, in the new interpretation of the depletion layer, a higher oxygen partial pressure provides electrons from inside the (P_{O2}(III)), producing more O^- and increasing $[O^-]/[e^-]$. This is thought to be due to the fact that the Fermi level is lowered by pkT. The bulk electron density then decreases with the shift in Fermi level.

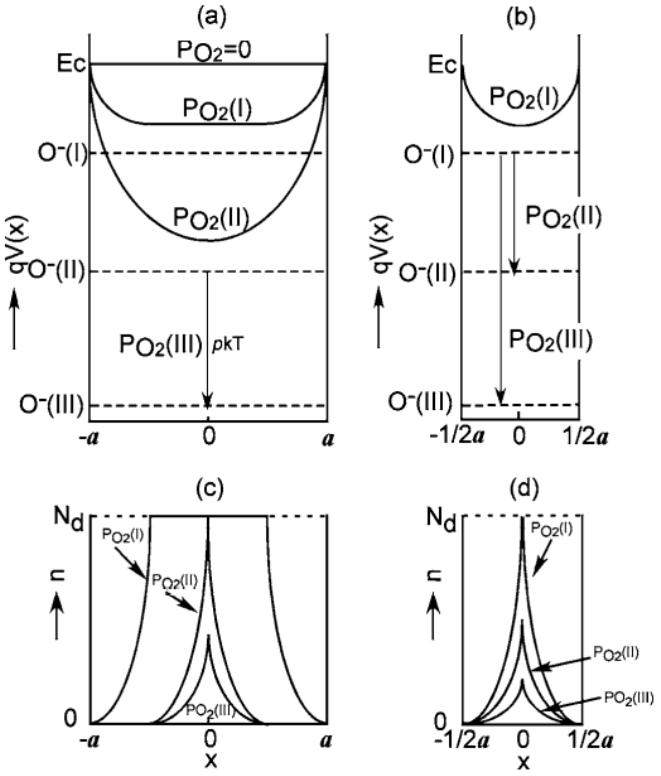

Fig.1.10 Schematic diagrams of the relationship between oxygen partial pressure and surface potential effect [36].

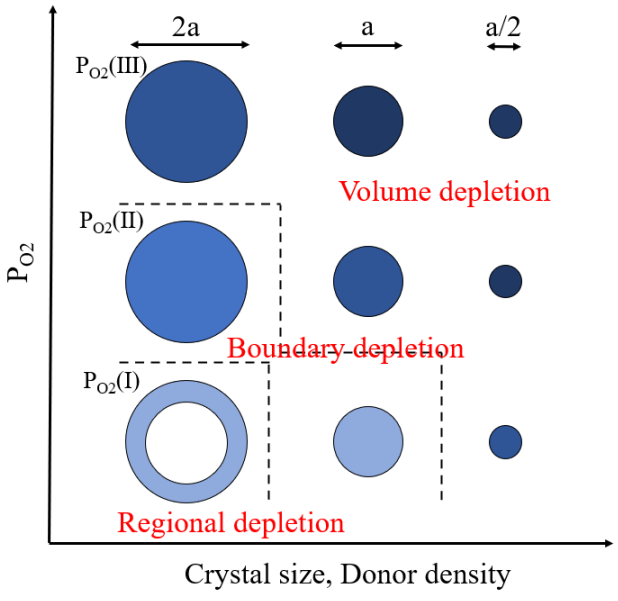

Fig.1.11 Depletion state change of spherical particles.

Figure 1.11 shows a schematic of the depletion layer state using a spherical particle model. It can be seen that the depletion changes from regional depletion to volume depletion as the oxygen partial pressure increases or as the particle size decreases. In the regional depletion region, the electrical resistance is expressed by the following equation.

$$R/R_0 = e^{\frac{m^2}{2}} \tag{1.6}$$

where m is the depletion depth, m=w/L_D, and R_0 is the resistance in the flat band state shown in Fig.1.10. On the other hand, in the volume depletion region, it is expressed by the following equation.

$$O_2 + 2e^- \underset{k_2}{\overset{k_1}{\rightleftarrows}} O_2^- \tag{1.7}$$

$$\frac{R}{R_0} = \left(\frac{3}{a}\right)(K_{O2}P_{O2})^{\frac{1}{2}} + const. \tag{1.8}$$

Next, a theoretical analysis of hydrogen sensitivity is described, where the response to hydrogen is based on the following [O^-] consumption rates

$$O^- + H_2 \underset{\leftarrow}{\overset{k_1}{\rightarrow}} H_2O \tag{1.9}$$

$$\frac{d[O^-]}{dt} = k_1P_{O2}[e] + k_{-1}[O^-]^2 - k_2P_{H2} \tag{1.10}$$

In the volume depletion region, the electrical resistance under hydrogen gas atmosphere is shown as follows.

$$R_g/R_0 = 3(X/n)/\{1 + (3/n)Y\}^{1/2} \tag{1.11}$$

$$X = (K_{O2}P_{O2})^{1/2},\ Y = (c/L_DN_d)P_{H2} \tag{1.12}$$

Then, using the electrical resistance Ra in air and defining the sensor sensitivity as R_a/R_g, the following equation is obtained.

$$R_a/R_g = (R_a/R_0)/(R_g/R_0) \tag{1.13}$$

$$R_a/R_g = 1 + \{(3c/aN_d)P_{H2}\}^{1/2} \tag{1.14}$$

It can be seen that the sensor sensitivity increases with decreasing particle size (2a) and donor density, and is proportional to the 1/2 power of the hydrogen partial pressure. This proportionality constant increases with decreasing donor density and particle size. The relationship between the depletion theory of semiconductors and gas surface interactions is explained by the development of a relationship between particle size and donor density. It is possible that a supported electron trap with acceptors may develop on the particle surface as well as on the semiconductor itself. The p-n junction formed by supporting acceptors could exhibit the same effect as a decrease in donor density and transition to volume reduction under low oxygen partial pressure.

1.3.3 Utility factor

Figure 1.12 shows the diffusion model of the sensor, assuming a porous thin film on an alumina substrate. Yamazoe et al. analyzed the gas diffusivity in the sensor membrane using the reaction-diffusion equation [40-42]. The SnO_2 particles used in the sensor are difficult to sinter, and even when sintered at 600 ºC, the crystallite diameter can be suppressed to 10-20 nm, suggesting that the pore size is in the mesopore region

and gas diffusion proceeds by Knudsen diffusion. Let the gas diffusion boundary condition be $C=C_s$ at x=0 and dC/Dx=0 at x=L. The film thickness dependence of gas diffusion in thin films can be obtained by using the reaction rate constant k and the Knudsen diffusion coefficient D_k from the diffusion equation for gases in porous materials.

$$C = C_s \frac{cosh\left\{(L-x)\times(\frac{k}{D_k})^{1/2}\right\}}{cosh\left\{L\times(\frac{k}{D_k})^{1/2}\right\}} \tag{1.15}$$

It can be seen that the gas concentration varies significantly with the value of k/D_k, indicating that the depth of gas penetration decreases with increasing values of k/D_k. Figure 1.13 shows how the gas concentration in the sensing film decreases in the depth direction (x) at steady state, assuming that the reaction rate is proportional to the gas concentration (C), which is related to the parameter $m=L(k/D_k)^{1/2}$.It can be seen that when the surface reaction rate is large and the diffusion coefficient is small, only the places near the extreme surface of the sensing film act as sensors. Studies using the gas diffusion equation show that the gas sensitivity is highly dependent on the film thickness, the gas diffusion coefficient and the reaction rate constant.

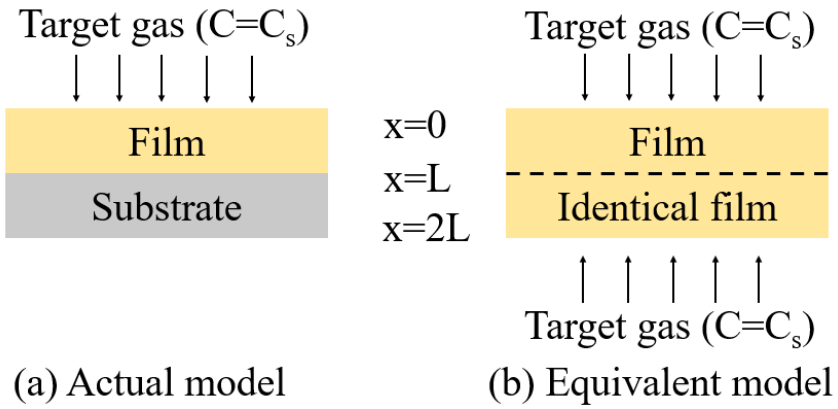

Fig.1.12 Diffusion model of thin film sensor.

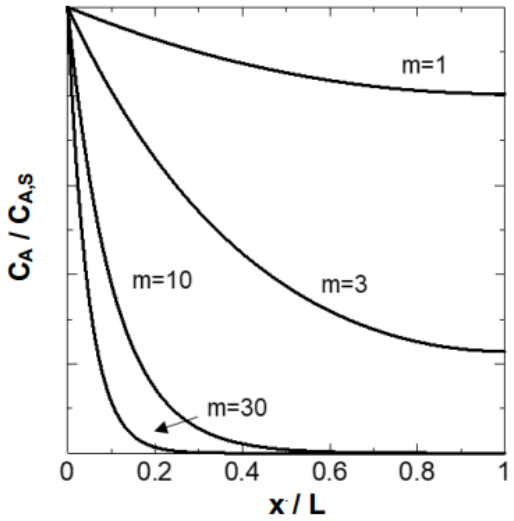

Fig.1.13 Variation of gas concentration with film thickness.

1.4 Role of the receptor

Metal oxides are rarely used on their own because of their weak acid-base properties. Therefore, they are often used as receptors. For this reason, most of them are used as composite oxides when used as catalysts. This involves the electronegativity and charge between different metals, and therefore, the acid-base properties are different from those of a single metal oxide. The highest acid strength in the case of composite oxides is correlated between the average partial charge of oxygen and the average electronegativity of the metal ions [43]. Previously, Jinkawa et al., investigated the relationship between ethanol gas sensitivity and surface catalytic properties of tin oxide sensors modified with acidic or basic oxides [44]. It was found that the addition of a basic oxide significantly enhanced the sensitivity to ethanol gas at 300°C, while the sensitivity hardly changed with the addition of an acidic oxide (WO_3). The incorporation of a basic metal oxide into SnO_2 improved not only the dehydrogenation of ethanol but also the consecutive oxidation of CH_3CHO to CO, as a result of enhanced catalytic activity. Conversely, the acidic metal oxide only enhanced the dehydration reaction and even had a negative impact on the consecutive oxidation. This phenomenon appears to be related with the reaction pathway of ethanol gas which are dependent on the acid–base properties of metal oxide catalysts.

The adsorbed oxygen is important for n-type semiconductors because the change in electrical resistance is generally observed due to the adsorption and desorption of surface adsorbed oxygen in air and in the test gas. Typical oxide semiconductors with adsorbed oxygen include SnO_2 and ZnO. The TPD results of oxygen from metal oxides has been reported by Iwamoto and Seiyama [45-47]. Table 1.2 shows the desorption of oxygen from metal oxides until 560°C. The 13 metal oxides no matter n/p type were divided into three groups, in group A, these oxides gave no significant desorption in the range 10-560°C, it is speculated that these oxides may have taken up adsorbed oxygen as lattice oxygen during temperature increase and did not desorb. Group B comprises transition metal oxides, it featured large amount of oxygen adsorbs and reacts actively.

The group C shows small amount of oxygen adsorbs and reacts mildly. In addition, the reactions give the change in electric resistance, so this group of materials is more suitable as a base material.

Table 1.2 Desorption of Oxygen from Metal oxides [45].

Group	Oxides	V_{560} (cm^3/m^2)
A	V_2O_5 (n)	0
	MoO_3 (n)	0
	Bi_2O_3 (p)	0
	WO_3 (n)	0
B	Cr_2O_3 (p)	2.13×10^{-2}
	MnO_2 (p)	6.54×10^{-2}
	Co_3O_4 (p)	3.30×10^{-2}
	NiO (p)	1.12×10^{-2}
	CuO (p)	1.42×10^{-1}
C	Fe_2O_3 (n)	4.05×10^{-3}
	TiO_2 (n)	5.52×10^{-5}
	ZnO (n)	2.45×10^{-4}
	SnO_2 (n)	2.11×10^{-3}

Figure 1.14 shows the energy band diagrams for grains different in size, but this model is also applicable for the interfacial contact between acidic oxide and SnO_2. As shown in the figure, the Fermi energy levels ($E_{F1(f)}$ and $E_{F2(f)}$) are located at different levels, or the grains have different values of the work function. When the grains are in touch, they should fulfill a critical requirement that the Fermi level be at the same level throughout the whole system. A very important phenomenon called pinning will occur, which is well recognized in contacts between metals and semiconductors. When the semiconductor is free of surface states, it should transfer electrons from or to the metal in order to establish equilibrium in between. Some heterojunction sensors have been reported [48].

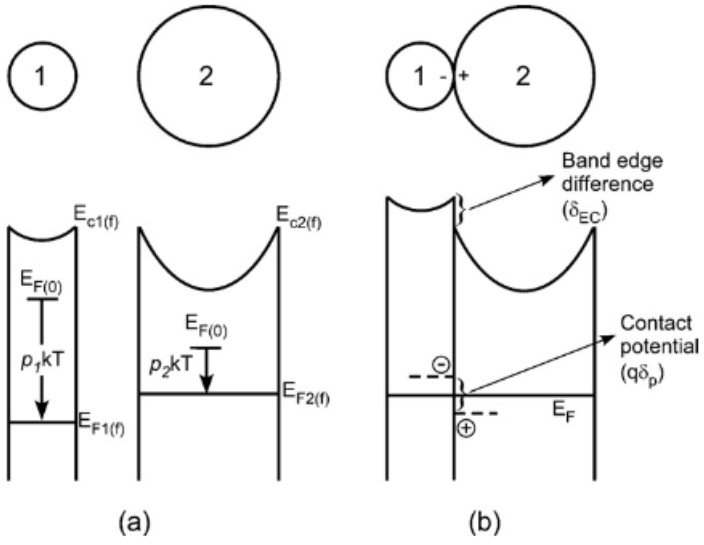

Fig.1.14 Energy band diagrams for grains different in size
(a) Free grains (b) Contacting grains [35]

In recent years, studies on WO_3 as receptor loaded metal oxide have been mostly reported. A summary is shown in Table 1.3. The researchers have loaded the acidic oxide (WO_3) for different morphologies of SnO_2 and have made some speculations on the mechanism based on the experimental results.

Table 1.3 A list of research for WO_3 loaded SnO_2.

·Author	Sensor materials	Sensor response	Detected gas	literature
Yin et al	WO_3-SnO_2 (nanosheet)	32.1 (260ºC, 50ppm)	Acetone	Journal of Alloys and Compounds 2018, Pages 322-331[49]
Zhu et al	WO_3-SnO_2 (nanosphere)	16.9 (240ºC, 1000ppm)	Acetone	Journal of Alloys and Compounds 2019, Pages 789-795[50]
VK Tomer et al	WO_3-SnO_2 (nanohybrids)	87 (220℃,50 ppm)	Triethylamine	Sensors and Actuators B 229 (2016) 321–330[51]
Nguyen V et al	WO_3-SnO_2 (nanofilms)	7.1 (300℃,250 ppm)	NH_3	Materials Science and Engineering: B 2017, 163-170[52]
Zhang et al	Pd-WO_3/SnO_2 (nanotubes)	65 (275℃,50 ppm)	Acetone	Sens. Actuators B Chem. 2020 127575[53]
Li et al	Pd-WO3/SnO2 (double layer)	38 (400℃,200 ppm)	NO	Sens. Actuators B Chem. 2015, 398-405[54]
Zhang et al	WO_3-SnO_2 (dual-layer)	29.31 (225℃,100 0 ppm)	Hydrogen	Ceramics International 2017, 6693-6699[55]
Hoa et al	WO_3-SnO_2 (nanowire)	177 (200 ℃,1 ppm)	H_2S	Materials Today Communications 2021, 102094[56]

Shao et al	Au@WO_3-SnO_2 (nanofibers)	79.6 (150 ℃,0.5 ppm)	Acetone	Applied Surface Science 2019, 902-911[57]

1.5 Motivation

SnO_2 is a widely used gas sensor material, and the SnO_2-based semiconductor gas sensors can be used to detect low concentrations of combustible gases such as volatile organic compound (VOC) gases. We propose three key factors for fabricating highly sensitive gas sensors: receptor function, transducer function, and utility factors. The receptor function is described in detail in subsection 1.1.3. In this study, WO_3 was loaded as receptor that does not produce negatively charged adsorbed oxygen in order to experimentally verify and simulate the chemo-sensitization of the receptor effect of acidic oxide (WO_3). Although Jinkawa et al. has been done the reaction paths of acid/base receptor-loaded SnO_2 with different acid bases, however, the relationship between the modification method and the sensor response is not clear. The particles size and its dispersity are strongly influenced by compositing method of receptor oxide, and should affect the receptor function. However, these receptor-related theories are not established well. Thus, this study focused on WO_3 as an acidic receptor and the receptor effect based on two WO_3 compositing methods on its sensing properties was investigated. Chapter 2 describes the preparation of sensor materials, the fabrication of sensor elements, and sensor measurement. In Chapter 3, the physical properties of the prepared material are evaluated. The variation of SnO_2, WO_3-SnO_2 resistance values in air and the response properties to H_2, CO, ethanol and acetone were investigated in Chapter 4. Chapter 5 summarizes the paper and the outlook for future research and concludes with acknowledgments.

2. Experiments

2.1 Introduction

In this chapter, neat and 1, 3, 5 mol% WO_3-SnO_2 nanoparticles were synthesized by hydrothermal treatment, impregnation method and mechanical mixing method. Porous gas-sensing layers were fabricated by screen printing and sensor devices were manufactured. In addition, the physical property evaluation method and sensor measurement method using the prepared sample are described. A list of chemicals used in the experiment is shown in table.2.1.

Table.2.1 A list of chemicals used in this experiment.

Chemicals	Chemical formula	Purity / %	Chemical company
Tin chloride pentahydrate	$SnCl_4 \cdot 5H_2O$	98	Fujifilm Wako Pure Chemical Corporation
Ammonium bicarbonate	NH_4HCO_3	20 - 23	Fujifilm Wako Pure Chemical Corporation
Ammonium nitrate	NH_4NO_3	98	Fujifilm Wako Pure Chemical Corporation
Tetramethylammonium hydroxide (TMAH)	$(CH_3)_4NOH$	15	Fujifilm Wako Pure Chemical Corporation
Sodium tungstate, 2-hydrate	$Na_2WO_4 \cdot 2H_2O$	99.0~100.5	KISHIDA CHEMICAL CO., LTD
Sulfuric Acid	H_2SO_4	95	Fujifilm Wako Pure Chemical Corporation
Ammonia Solution	NH_3	28	Fujifilm Wako Pure Chemical Corporation
Hydrogen peroxide	H_2O_2	30	Fujifilm Wako Pure Chemical Corporation
α-Terpineol	$C_{10}H_{18}O$	98	Fujifilm Wako Pure Chemical Corporation

2.2 Experimental Details

2.2.1 Synthesis of SnO_2 nanoparticles

Figure.2.1 shows the flowchart of the preparation of SnO_2 nanoparticles by hydrothermal treatment and calcination. Using Tin (IV) chloride pentahydrate ($SnCl_4 \cdot 5H_2O$) solution and ammonium bicarbonate (NH_4HCO_3) solution as starting materials (ratio at 1:5), and ammonium nitrate (NH_4NO_3) as co-precipitant. Stannic acid gel ($SnO_2 \cdot nH_2O$) was prepared by adding an $SnCl_4 \cdot 5H_2O$ solution (1M) into an

NH_4HCO_3 solution (1M) dropwise. Cl^- was removed by washing the obtained white precipitate for 10 times (centrifugation: 3500 g, 10 min, 15°C), and a gel was formed while NH_4NO_3 was removed by 2 times high-speed centrifugation (12000 g, 10 min, 15°C), the gel was washed and then dispersed into de-ionized water. The pH of the dispersion was adjusted to 10.5 through the addition of tetramethyl ammonium hydroxide (TMAH), thereafter the dispersion was hydrothermally treated at 200°C for 10 hours using a stainless reaction vessel with PTFE inner cylinder. The obtained solution with SnO_2 nanocrystals was distillated and dried at 80°C for 2 hours. And calcined at 600°C for 3 hours under dry/wet O_2 flow to obtain the SnO_2 nanoparticles.

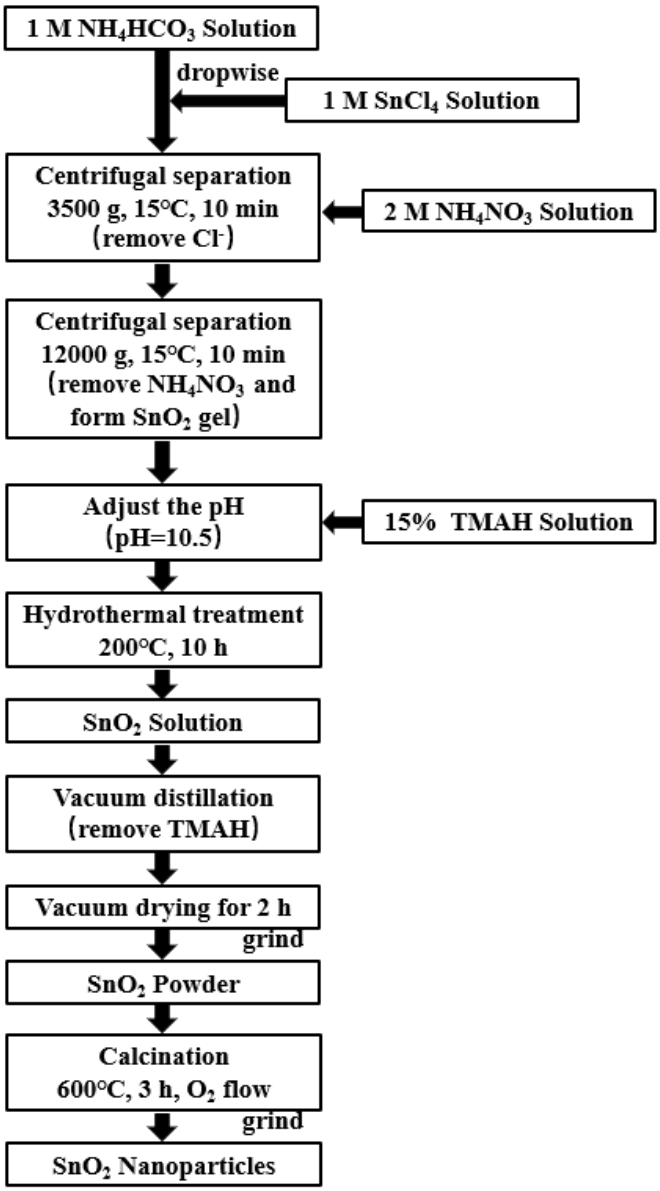

Fig.2.1 Flowchart of the preparation of SnO_2 nanoparticles by hydrothermal treatment and calcination.

2.2.2 Synthesis of WO_3 particles

Figure.2.2 shows the flowchart of the preparation of SnO_2 nanoparticles by acidification method. The synthesis of WO_3 was carried out according to the previous methods of our laboratory [58].

The acidification method was used to synthesize WO_3 nanoparticles with a lamellar- structure. A sodium tungstate dihydrate (Na_2WO_4) solution (0.5 M, 50 mL) was added drop by drop to a sulfuric acid (H_2SO_4) solution (pH=−0.8, 300 mL) under vigorous stirring. The quick mixing led to the formation of a yellow suspension containing crystalline $WO_3 \cdot nH_2O$, which was left to age for 24 hours at 30°C. The particles were extensively washed with distilled water to remove Na^+ through centrifugation (12000 g, 10 min, 15ºC) until the supernatant solution reached a pH of 5−6. After drying at 80ºC, the final powders were obtained and calcined at 500ºC under wet O_2 for 2 h.

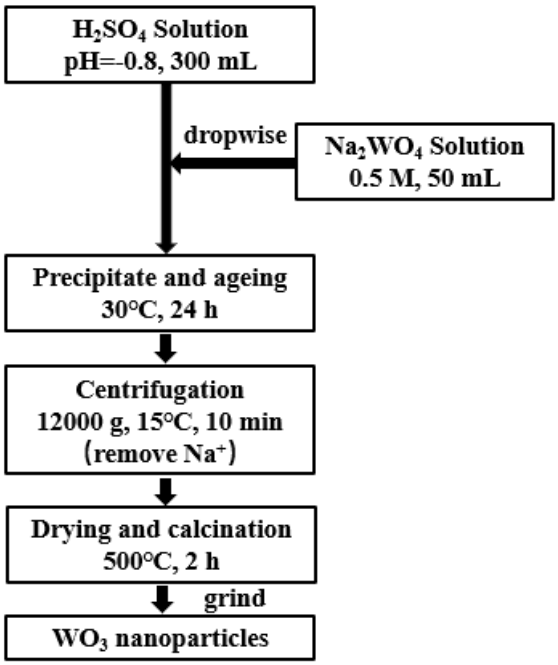

Fig.2.2 Flowchart of the preparation of SnO_2 nanoparticles by acidification method.

2.2.3 Synthesis of WO_3-SnO_2 nanoparticles

Figure.2.3 shows the flowchart of the preparation of WO_3-SnO_2 nanoparticles. This time, two loading methods were used, which are standard process ((a) impregnation method) and mechanical mixing method, respectively. For loading, it is known from previous data that the crystallite size of WO_3 particles is larger than that of

SnO_2 and tend to agglomerate when loaded, so wet-SnO_2 should be used because it is easier to be loaded.

For the impregnation method, the appropriate ratio (1, 3, 5 mol%) of WO_3 (before calcination) solution (10 mL) was added drop by drop to a mixture by SnO_2 powder (1 g) with deionized water (20 mL) under stirring and then stirred for 24 h. After centrifugation (12000 g, 15°C, 10 min) and drying, the WO_3 loaded SnO_2 powder was obtained after sintering under a wet oxygen flow at 500℃ for 2 hours. This group of materials is called loading group. On the other hand, for the mechanical mixing method, the appropriate ratio (1, 3, 5 mol%) of WO_3 powder (after calcination) was mechanically mixed with the SnO_2 powder for 15 min to obtain WO_3-mixed SnO_2 nanoparticles. And this group of materials is called mixing group.

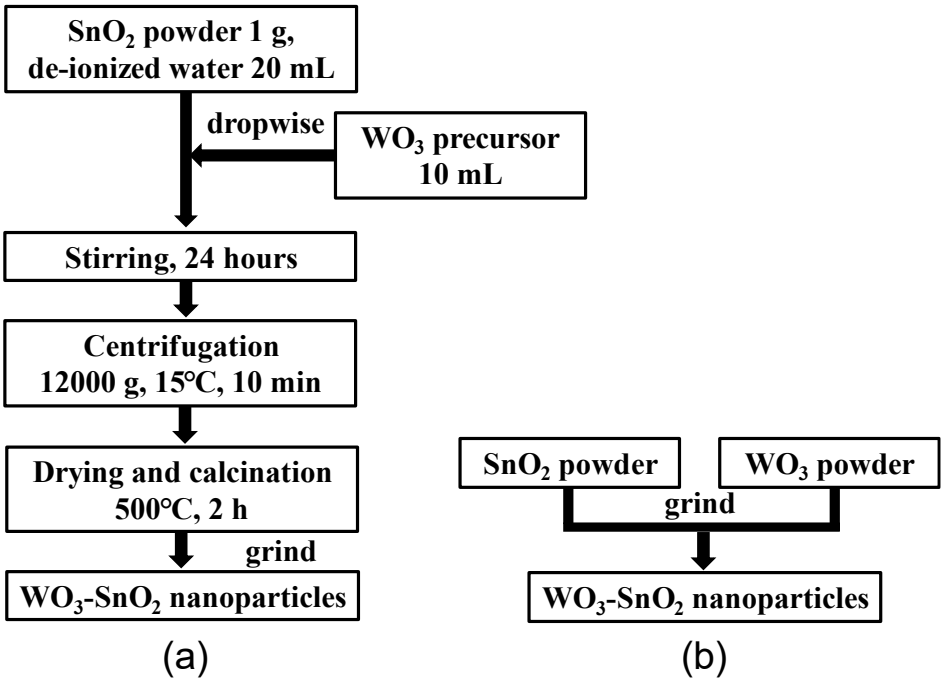

Fig.2.3 Flowchart of the preparation of WO_3-SnO_2 nanoparticles
(a) Impregnation method, (b) Mechanical mixing method.

2.3 Material Evaluation

2.3.1 X-ray diffraction (XRD) method and calculation of crystallite size

Identify the compounds of the samples prepared in 2.2.1, 2.2.2 and 2.2.3 by X-ray diffraction. X-ray diffraction measurements used a benchtop X-ray diffractometer (Rigaku Co., Ltd., Mini Flex). The X-ray source of measurement conditions is CuKα (40kV, 30mA), the scanning speed is 2.0°/min, the scanning step is 0.02°, and the scanning range is $2\theta=10^{o}\sim80^{o}$. Furthermore, compounds were identified against the obtained XRD patterns.

From the obtained peaks, the crystallite size was determined by using Scherrer's equation [59].

$$D_{hkl} = \frac{K \cdot \lambda}{\beta cos\theta} \text{(Scherrer's equation)}$$

Where D denotes mean crystalline size, K is known as the Scherer's constant (K=0.9), the symbol β stands for the full width at half maximum of the peak, λ represents the wavelength of the X-ray (0.15418 nm), and θ is the center angle of the peak. In this paper, the crystallite size of the SnO_2 main peak (110), (101), (211) in the vertical direction is calculated, and the average value is taken to obtain the SnO_2 crystallite size.

2.3.2 Specific surface area and pore distribution by BET and BJH method

The specific surface area and pore distribution of the prepared powder samples were evaluated using an automatic specific surface area/pore distribution measurement device (BELSORP-mini II, manufactured by Nippon Bell Co., Ltd.). First, an appropriate amount of the powder sample (0.3 g) was measured in a sample tube, and after a decompression heat treatment (in vacuum: ~10^{-2}kpa, 300 °C) to remove adsorbates on the sample surface as a pretreatment, the sample was weighed accurately again. Nitrogen was used as the adsorbent, the adsorption temperature was 77 K, and the partial pressure ratio P / P_0 (equilibrium pressure divided by saturation vapor pressure) = 0 to 1, and the changes in pressure and adsorption amount were measured. In this study, specific surface area and pore distribution were derived by the BET and BJH methods.

2.3.3 Observation by Field Emission Scanning Electronic Microscopy (FE-SEM)

In order to observe the morphology of the prepared SnO_2, WO_3 and WO_3-SnO_2 powder, observation was performed with a field emission scanning electron microscope (FE-SEM, Field Emission Scanning Electron Microscope, SEM-IT800SHL). A carbon tape was attached to the SEM observation holder, and a small amount of powder sample was taken using a spatula and placed on the holder. Meanwhile the doping distribution of WO_3-SnO_2 was analyzed by X-ray energy-dispersive spectroscopy (EDS, SM-6701FMW) for the elements.

2.3.4 Observation of sensor film thickness by laser microscope

Using a shape analysis laser microscope (KEYENCE, VK-X1000), the fabricated sensor element was observed at 500 times magnification to evaluate the thickness of the sensor film. Structural analysis of the gold electrode was also performed.

2.4 Manufacturing of sensor element

Figure.2.4 and 2.5 show the flowchart of the fabrication of the sensor element and a schematic diagram of the sensor device, respectively. First, the surface of the

commercially available alumina substrate (13 x 9 x 0.5 mm Fine Ceramics Co., Ltd.) was cleaned with acetone and dried in a dry box set at 100ºC for 30 minutes. The Au paste was coated on the alumina substrate in a comb shape using a screen printer (MITANI ELECTRONICS, MEC-2400). This was calcined in a box-type electric furnace (S-70, manufactured by Denken Co., Ltd.) at 850ºC for 3 hours to obtain an alumina substrate with a comb-shaped gold electrode. Before the application of sensor materials, the substrate was cleaned with a mixed solution of H_2O_2, aqueous ammonia, and purified water in a ratio of 2:1:10 to remove organic impurities on the surface of the alumina substrate. After standing still for about 30 minutes, the generation of air bubbles decreased, and the aluminum oxide substrate with gold electrodes was taken out. The removed alumina substrates with gold electrodes were gently rinsed with purified water and dried in a dryer oven set at 100°C for 30 min.

The paste for applying the sample powder was then prepared. An appropriate amount of α-Terpineol was added as an organic binder to SnO_2 powder and mixing thoroughly to form a paste. This paste was coated on an alumina substrate with gold electrodes and dried at 120°C for 1 hour. After that, a platinum wire was wound around the two holes of the alumina substrate, and gold paste was further coated on the contact part between the sensor substrate and the platinum wire to form a sensor device (Fig. 2.5).

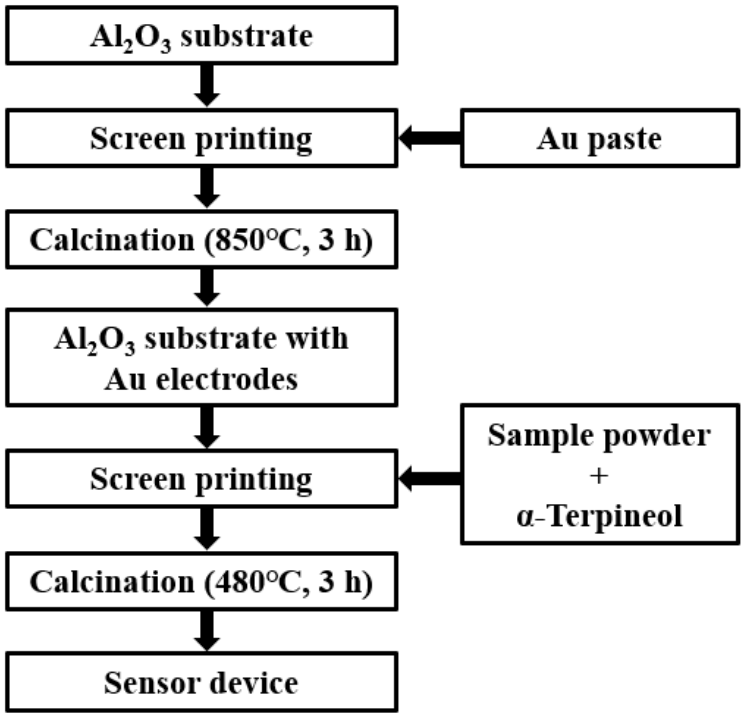

Fig.2.4 Flowchart of the fabrication of the sensor element.

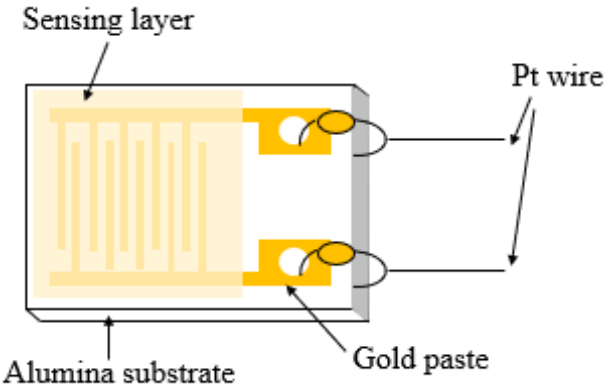

Fig.2.5 A schematic diagram of the sensor device.

2.5 Evaluation method for sensor characteristics

2.5.1 Resistance measuring device

Figure.2.6 shows the electric circuit for measuring the resistance of the sensor element. Figure.2.7 shows the schematic diagram of the resistance value measuring device. The fabricated sensor element was placed in the sample holder of the measurement unit, and the change in the resistance value of the element was measured. The applied voltage was set to 4V, and the electrical resistance value of the sensor element was calculated from the voltage applied to the reference resistor r. Here, the sensor resistance R is determined by the following formula, where E is the applied voltage, r is the reference resistance, V is the voltage applied to the reference resistance, and R is the resistance of the sensor element. From this formula, the resistance R of the sensor element was calculated by substituting each value.

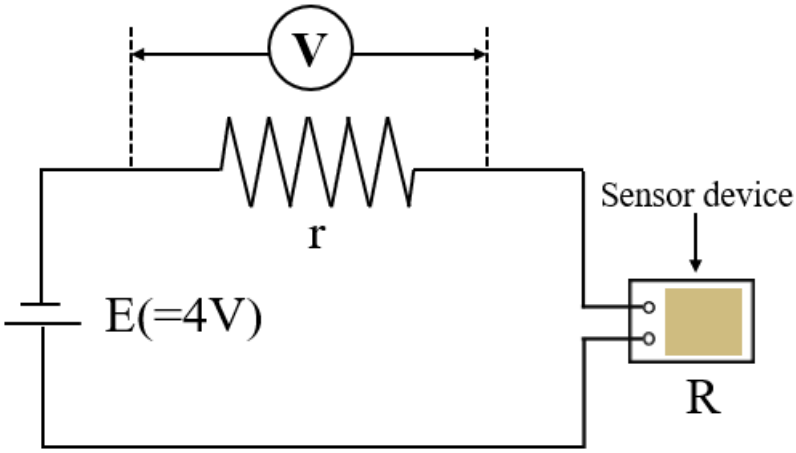

Fig.2.6 The electric circuit for measuring the resistance of the sensor element.

$$R = r \times (E/V - 1)$$

V: Output Voltage

E: Applied Voltage

r: Reference Resistance
R: Element Resistance

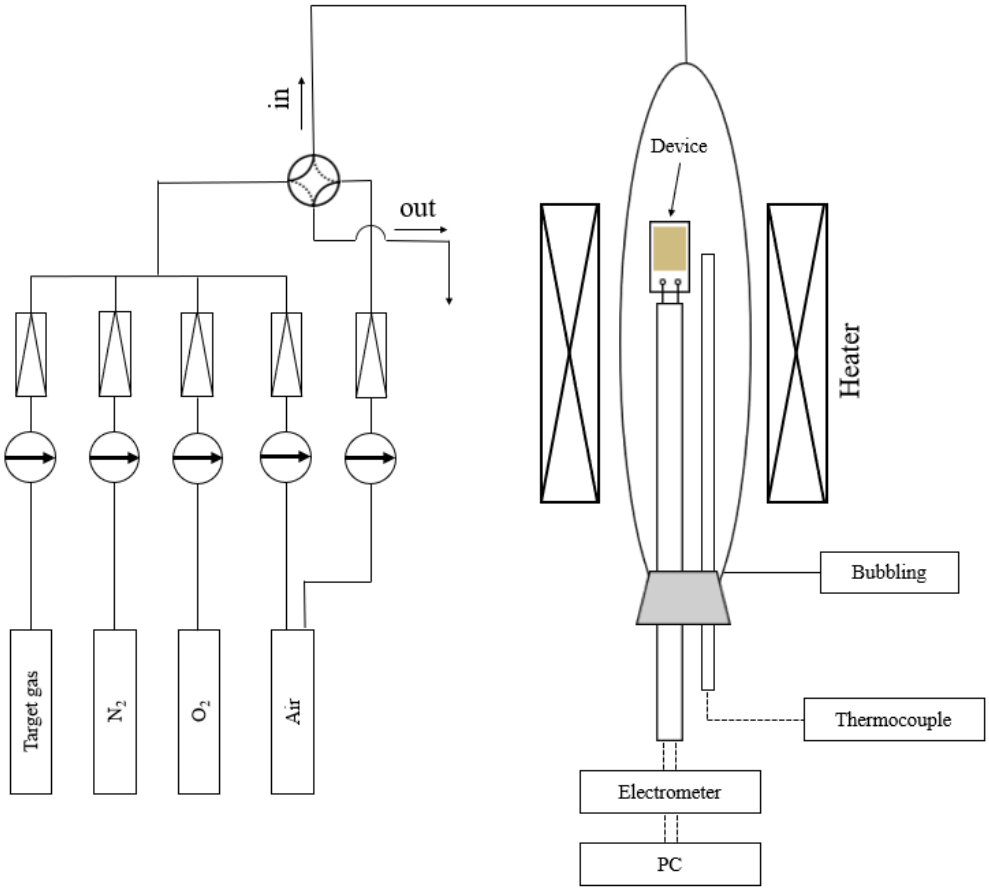

Fig.2.7 Schematic diagram of the electrical resistance value measuring device.

2.5.2 Pretreatment of the sensor element

Figure.2.8 shows the pretreatment before sensor measurement. The resistance value of the device and the sensor sensitivity are not only the results of measuring the gas ambient, but also the combined effect of interfering gases in the atmosphere. When the sensor element is exposed to the air, it will absorb water vapor, combustible gas, carbon dioxide (CO_2), nitrogen oxides (NO_x), etc. contained in the air. In this study, we evaluated the sensor response characteristics for single target gas. Therefore, before measuring the resistance value, it is necessary to remove the adsorbent on the surface of the sensor element by pretreating the sensor element. If the pretreatment temperature is too high, the oxygen in the SnO_2 lattice will desorb, causing the crystal structure to collapse and the material to become energetically unstable. From the TPD results of SnO_2, it was determined that oxygen in the lattice starts to desorb from around 600°C. In order to ensure the desorption of hydroxyl groups, the pretreatment temperature was set to 480°C, which is 20 degrees lower than the calcination temperature. The

temperature was raised from room temperature to the pretreatment temperature of 480°C at a rate of 2°C/min, kept for 3 hours, and then cooled to the desired measurement temperature at a rate of 2°C/min.

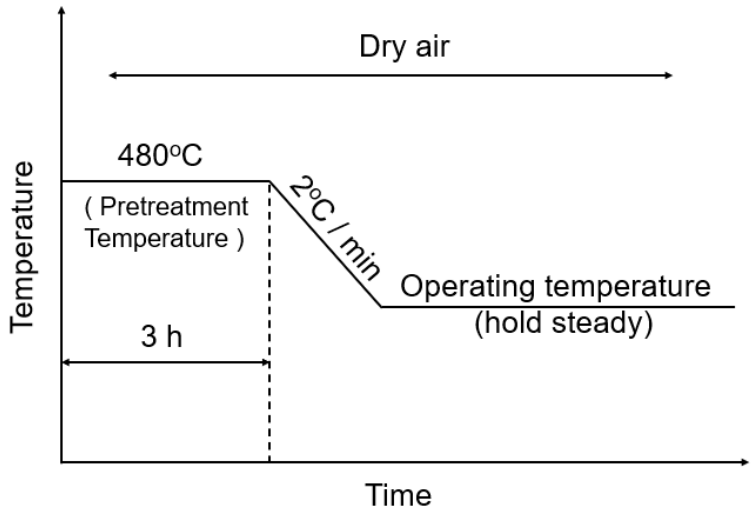

Fig 2.8 Schematic diagram of pretreatment of sensor measurement.

2.5.3 Evaluation of response characteristics for target gas

The semiconductor gas sensor detects the gas by calculating the ratio of the resistance value in the air (R_a) to the resistance value in the target gas (R_g). Here, the sensitivity S of the tested gas is defined as the ratio of the resistance value R_a to R_g (R_a/R_g).

In this study, response characteristics to H_2, CO, ethanol and acetone were evaluated. The sensor measurements were performed under dry atmosphere at operating temperatures of 350°C, 300°C,250°C and 200°C. At these temperatures, the concentration of H_2 and CO was 200 ppm and the concentration of ethanol and acetone was 20 ppm. A gas mixture containing H_2 (997 ppm), CO (1960 ppm) and ethanol (105.5 ppm) based on air was diluted with synthetic air, and a gas mixture containing acetone (136.6 ppm) based on nitrogen was diluted with O_2 and N_2 so that the total flow rate was 100 mL/min.

Table.2.2 Conditions for sensor measurement.

Operating temperature	350°C, 300°C, 250°C, 200°C	
Target gas	H_2, CO	Ethanol, Acetone
Concentration	200 ppm	20 ppm
Gas flow	100 mL/min	

2.6 Summary

In this chapter, sample preparation and evaluation methods and measurement methods are described. First, the preparation methods of the sensor materials, SnO_2, WO_3, and WO_3-SnO_2 are described, and the methods for evaluating their physical properties are presented. Next, methods of fabricating sensor measurement elements and sensor measurement methods using these prepared materials are described. Chapter 3 shows the evaluation of the prepared sensor materials and Chapter 4 shows the results of the sensor characteristics of the devices prepared in this chapter.

3. Characterization of SnO_2 and WO_3-SnO_2 nanoparticles

3.1 Introduction

In Chapter 1, the mechanism of metal oxide semiconductor sensors is introduced and three key factors to improve the performance are described, which are receptor function, transducer function and utility factor. In particular, the effects of receptors are described. The preparation of materials and sensor devices and performance testing methods are introduced in Chapter 2. In past studies, the relationship between electronegativity and sensitivity based of various acceptors was reported, but there was no detailed test description for the physical properties of materials.

In this chapter, we first attempted to synthesized SnO_2 and WO_3-SnO_2 nanoparticles by hydrothermal treatment, impregnation method and mechanical mixing method. Based on these preparation methods, the surface state, morphology and pore distribution of the obtained nanoparticles were evaluated in order to use the results as a basis for some reasonable analysis in combination with the gas sensing properties obtained in Chapter 4.

3.2 Characteristics of SnO_2 and WO_3-SnO_2 nanoparticles

3.2.1 X-ray diffraction patterns

First, the XRD patterns of dry-SnO_2 and wet-SnO_2 are shown in Figure 3.1. The XRD patterns were consistent with that of the rutile-type SnO_2 nanoparticles (ICSD 92552). No impurity was seen in the patterns.

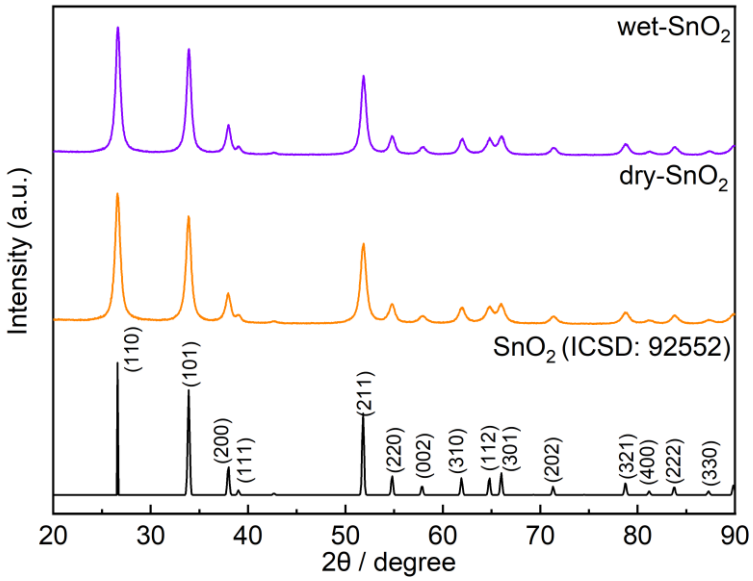

Fig.3.1 XRD patterns of dry-SnO_2 and wet-SnO_2.

Subsequently, the crystallite size after sintering under dry and wet oxygen flow was also investigated. The crystallite size of the products was calculated by Scherrer's formula are shown in Table 3.1. The average crystallite size of SnO_2 before calcined, dry-SnO_2 and wet-SnO_2 are each 3.7 nm, 8.18 nm and 14.66 nm, respectively. It can be inferred from the results that during calcination in wet oxygen flow, the crystal growth of SnO_2 particles was promoted by introducing water vapor. The reason for this result may be due to the separation of OH groups is easier than separation of O double bonds. Moreover, for loading, wet-SnO_2 should be used, because that the crystallite size of WO_3 particles is larger than that of SnO_2 and tend to agglomerate when loaded, so WO_3 may be more easily loaded on wet-SnO_2.

Table 3.1 Crystallite size of SnO_2.

Sample	2θ (deg.)	Crystal plane	Crystallite size (nm)	Average (nm)
SnO_2 (before calcined)	26.824	110	3.5	3.7
	33.992	101	3.7	
	65.56	211	3.9	
dry-SnO_2	26.605	110	8.07	8.18
	33.923	101	8.30	
	51.817	211	8.19	
wet-SnO_2	26.602	110	14.43	14.66
	33.870	101	15.06	
	51.803	211	14.49	

Figure 3.2 shows the phase structures of WO_3 nanoparticle powders are characterized by the X-ray diffraction. The sample exhibited the same pattern corresponding with the monoclinic WO_3 (ICSD 17003). By sintering at 500 ºC for 2 h under wet O_2, the crystalline size determined from the peak (002), (020) and (200) are each 23.72 nm, 24.24 nm and 30.11 nm, respectively.

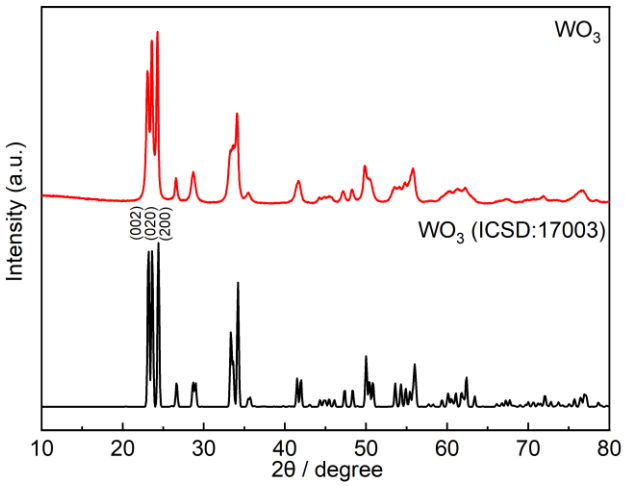

Fig.3.2 XRD patterns of WO_3.

Here, the sample characterization of SnO_2-WO_3 is shown in Figure 3.3. For 1 mol% loading/mixing, the sample exhibited the same pattern corresponding with the rutile-type SnO_2 nanoparticles (ICSD 92552) and there were no visible changes with WO_3-loading. This could be due to the small loading amount for the detection of XRD or the fine dispersion of WO_3 on the surface. But under the loading ratio of 3 mol% and 5 mol%, the (002), (020) and (200) peaks of WO_3 can be detected by XRD patterns. But through the results showed by table 3.2, the addition of WO_3 does not change the crystallite size. The figure below can more clearly show the peak of WO_3 under each loading and mixing.

However, on the right side of Figure 3.3, a very clear peak shift to low angle can be observed, and the shift angle for the loading group was slightly larger than that of the mixing group. The ionic radius of W^{6+}(0.60Å) is smaller than that of Sn^{4+}(0.69 Å), and for the loading method, W can be easily doped into the SnO_2 lattice at low amount, which corresponds to the XRD pattern. Moreover, it can be seen from the lattice constants that the lattice constants show an increasing trend compared to neat SnO_2 as the loading amount of WO_3 increases, both in group loading and mixing, and the increase of group loading is larger than that of group mixing. Therefore, the successful loading of WO_3 leads to the increase of the lattice constant and also leads to the shift of the XRD peak. Thus, it can be considered W was doped into the SnO_2 lattice and cation doping can have an effect on electrical properties.

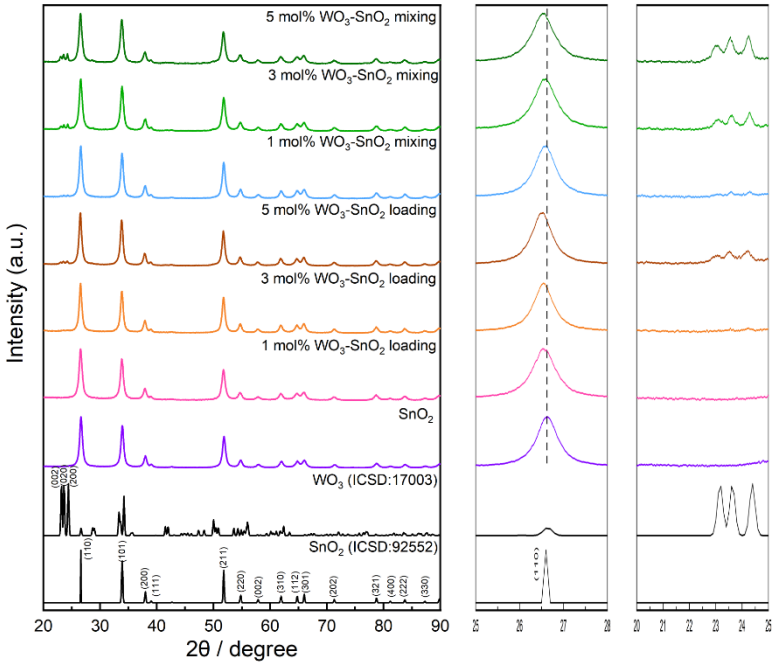

Fig.3.3 XRD patterns of neat-SnO_2, 1 mol%, 3 mol%, and 5 mol% WO_3-SnO_2 each by loading and mixing, respectively.

Table 3.2 Crystallite size for SnO_2 and each WO_3-SnO_2 by loading and mixing.

Sample	2θ (deg.)	Crystal plan e	Crystallite size (nm)	Average (nm)
SnO_2	26.578	110	13.39	13.55
	33.870	101	13.80	
	51.803	211	13.47	
1 mol.% WO_3-SnO_2 (loading)	26.533	110	12.92	13.37
	33.802	101	13.87	
	51.707	211	13.32	
3 mol.% WO_3-SnO_2 (loading)	26.519	110	15.35	15.37
	33.802	101	15.38	
	51.719	211	15.39	
5 mol.% WO_3-SnO_2 (loading)	26.482	110	14.95	15.20
	33.756	101	15.27	
	51.676	211	15.38	
1 mol.% WO_3-SnO_2 (mixing)	26.572	110	14.35	14.39
	33.832	101	14.32	
	51.754	211	14.50	
3 mol.% WO_3-SnO_2 (mixing)	26.558	110	13.02	13.11
	33.836	101	13.06	
	51.742	211	13.26	
5 mol.% WO_3-SnO_2 (mixing)	26.511	110	13.23	13.23
	33.780	101	13.02	
	51.677	211	13.46	

Table.3.3 Lattice constant of neat-SnO_2, 1 mol%, 3 mol%, and 5 mol% WO_3-SnO_2 each by loading and mixing, respectively.

Lattice constant	a(Å)	c(Å)
SnO_2	4.7378	3.1864
1 mol% WO_3-SnO_2 (loading)	4.7429	3.1905
3 mol% WO_3-SnO_2 (loading)	4.7380	3.1868
5 mol% WO_3-SnO_2 (loading)	4.7394	3.1875
1 mol% WO_3-SnO_2 (mixing)	4.7408	3.1889
3 mol% WO_3-SnO_2 (mixing)	4.7411	3.1879
5 mol% WO_3-SnO_2 (mixing)	4.7415	3.1888

3.2.2 Specific surface area and pore distribution by BET and BJH method

The surface areas and porous structures of fabricated NPs were evaluated by nitrogen adsorption–desorption method. Figure 3.4 shows the (a) N_2 adsorption/desorption isotherms and (b) pore diameter distribution of wet-SnO_2 evaluated by BJH method. The specific surface area and pore volume are each 17.2 $m^2 \cdot g^{-1}$ and 0.052 $cm^3 \cdot g^{-1}$, respectively. The nanoparticles were porous and had nanosized pores with average diameters of approximately 12.2 nm.

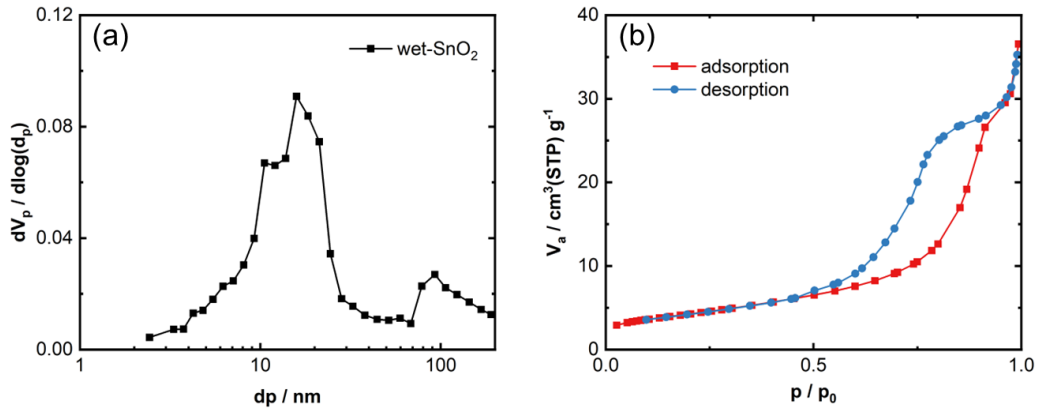

Fig.3.4 (a) N_2 adsorption and desorption isotherms and (b) pore diameter distribution of wet-SnO_2.

According to Fig.3.4(b) and Fig3.5, all the adsorption-desorption isotherms show type IV, which corresponds to a system with capillary condensation of the porous adsorbent, reflecting a relatively uniform pore size distribution.

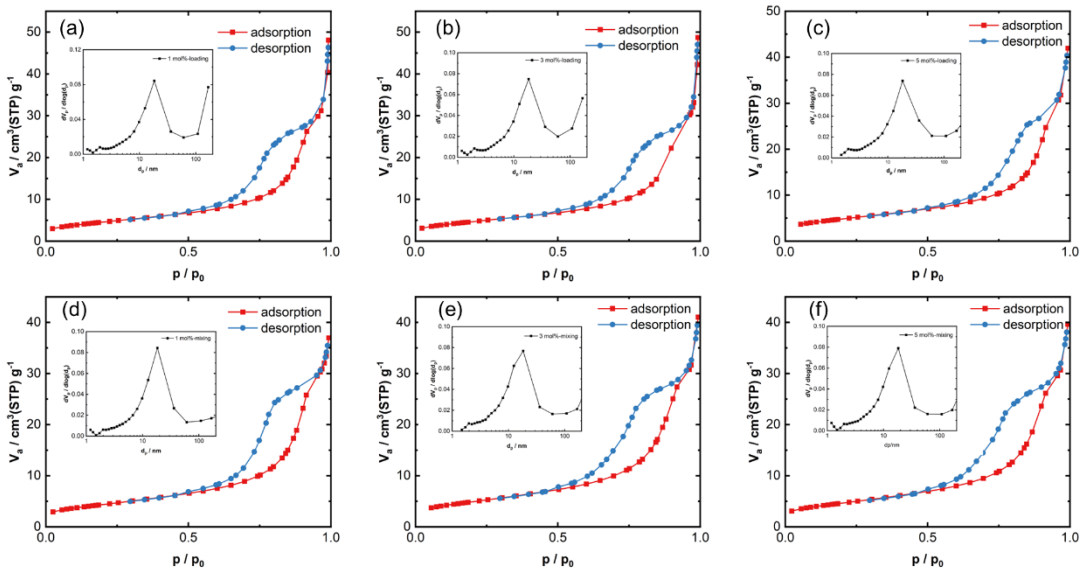

Fig.3.5 (a) N_2 adsorption and desorption isotherms and pore diameter distribution of (a)~(f) 1%, 3%, and 5 mol% WO_3-SnO_2 each by loading and mixing, respectively.

The BJH surface areas, pore volume and average pore diameter of all samples are listed in Table.3.4. The BJH surface areas of all NPs are in the range of 17.2-18.9 m^2/g. The pore volume and average pore diameter increase slightly with the increase of WO_3 content and the increase of the loading group is slightly higher than that of the mixing group. Although these data have slight changes, they are still very similar, and it is difficult to think that this will be the key factor for the change of gas sensing properties.

Table.3.4 Surface areas, pore volume and average pore diameter of seven as-prepared NPs.

	Specific surface area / $m^2 \cdot g^{-1}$	Pore volume / $cm^3 \cdot g^{-1}$	Average pore diameter / nm
neat-SnO_2	17.2	0.052	12.2
1 mol%-loading	18.7	0.064	13.6
3 mol%-loading	18.5	0.062	13.3
5 mol%-loading	18.3	0.06	14.1
1 mol%-mixing	17.8	0.055	12.4
3 mol%-mixing	18.3	0.059	12.9
5 mol%-mixing	18.9	0.057	12.2

3.2.3 Morphology observation by FE-SEM and SEM-EDS

The sample nanoparticle powders were analyzed by FE-SEM. Figure 3.6 (a) shows that although SnO_2 particles are easy to agglomerate, it can still be seen that the particles are nanoscale. From the high magnification SEM image of Fig.3.5 (b), the sample powder consists of a numerous of irregular lamellar-structured particles, and it is estimated that the lateral size is around 100-200 nm with a thickness 10-30 nm.

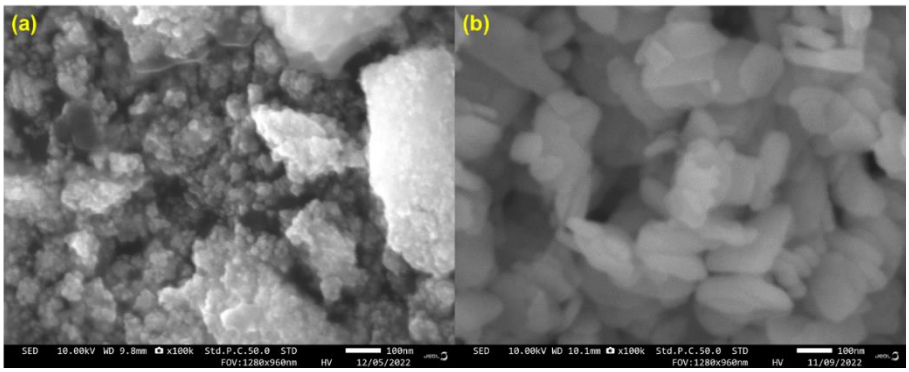

Fig.3.6 FE-SEM images of (a) SnO_2 and (b) WO_3 particles.

Figure 3.7 shows the FE-SEM images of 1, 3, 5 mol% WO_3-SnO_2 (a), (b), (c) loading group and (d), (e), (f) mixing group, respectively. For the WO_3-SnO_2 loading group, it can be seen that the WO_3 particles evenly distributed among the SnO_2 particles. On the other side, for the mixing group, it can be clearly seen that the lamellar-structured WO_3 particles and SnO_2 are agglomerated together irregularly. Both particles are packed together and form a large mesoporous structure, which is very important for penetration of gas molecules in the gas-sensing layer. [57,60-62]

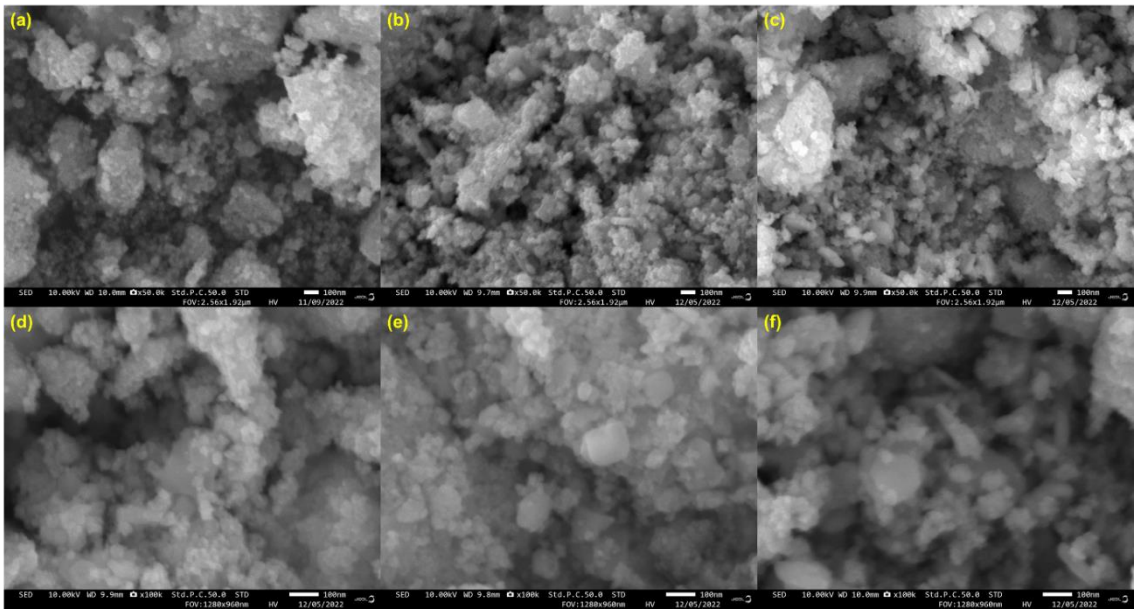

Fig.3.7 FESEM images of 1, 3, 5 mol% WO_3-SnO_2 (a), (b), (c) loading group and (d), (e), (f)mixing group, respectively.

Next, Figure 3.8 shows the SEM image of (a) WO_3-loaded SnO_2 and (b) WO_3-mixed SnO_2 used as a comparative material, and the results of elemental analysis by EDS.

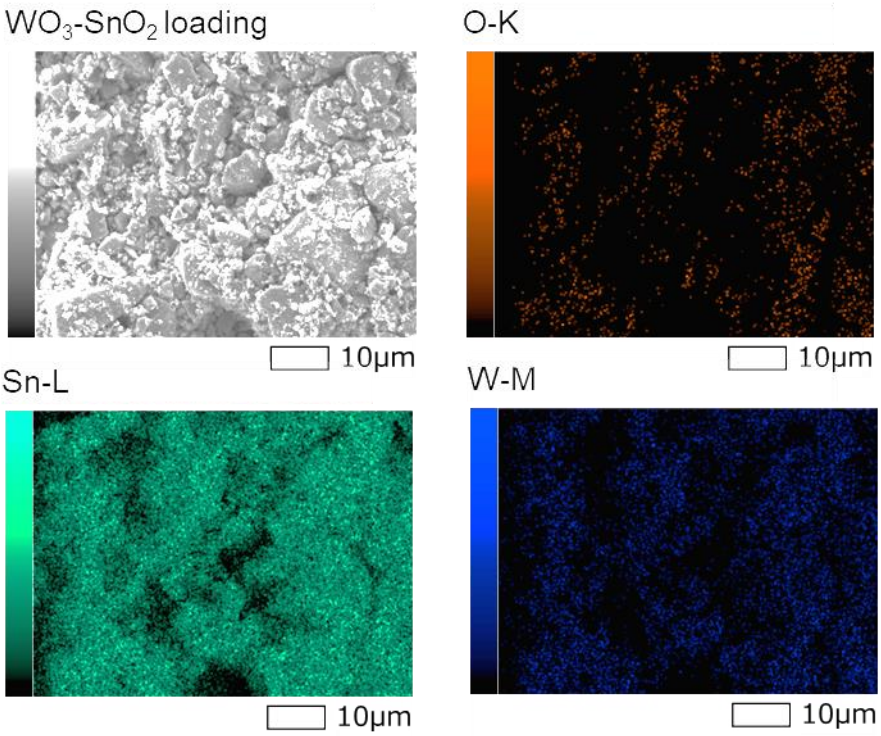

Fig.3.8 (a) SEM image and corresponding EDS mapping of Sn, W and O elements of 1 mol% WO_3–SnO_2 NPs (loading group).

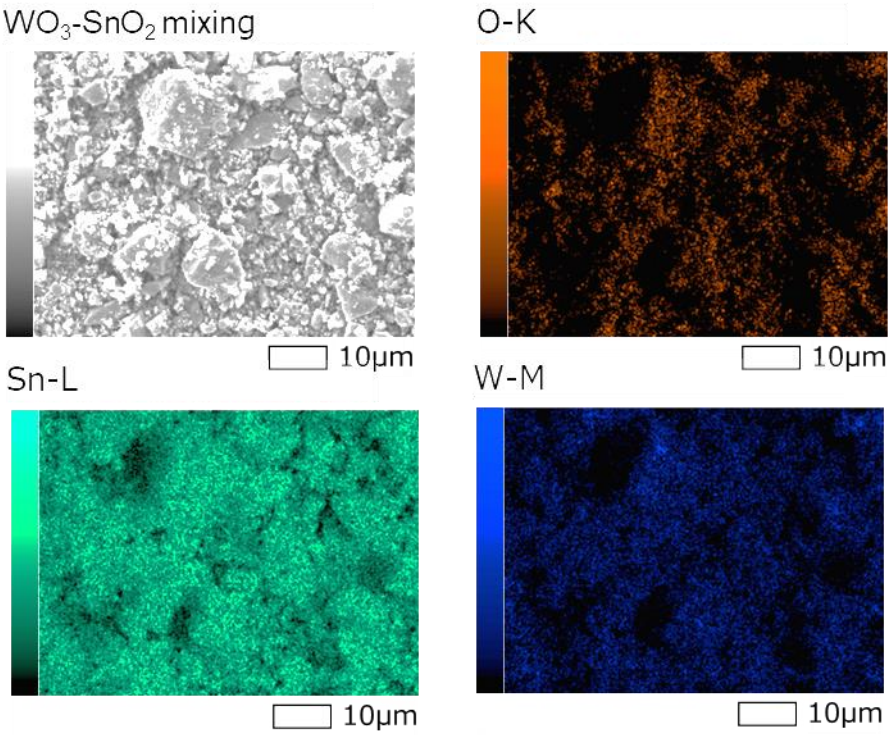

Fig.3.8 (b) SEM image and corresponding EDS mapping of Sn, W and O elements of 1 mol% WO_3–SnO_2 NPs (mixing group).

According to the results of EDS spectra, even if the addition of WO_3 is 1 mol%, W can be detected, and the distribution of Sn, W and O elements in the whole sample area is uniform, which confirms that these elements are well dispersed in WO_3-SnO_2 NPs. At the same time, it can be seen from the comparison of EDS spectra that compared with the WO_3-loaded SnO_2, the WO_3 particles in the WO_3-SnO_2 are dispersed as fine particles.

3.2.4 Observation of the thickness of sensor film

The gold substrate with comb electrodes and the film thickness of the sensor element after sample coating were evaluated. Using the base on the alumina substrate as the reference plane, the film thickness was measured at three locations on the sensor device, and the average thickness and spacing are summarized in Table 3.5. The results show that the average thickness and interval of the Au electrode was about each 6.8 μm and 72.3 μm, respectively. Table 3.6 summarizes the average film thickness of the sensor elements. The measurement results show that the average thickness of the sensor film was about 30-40 μm.

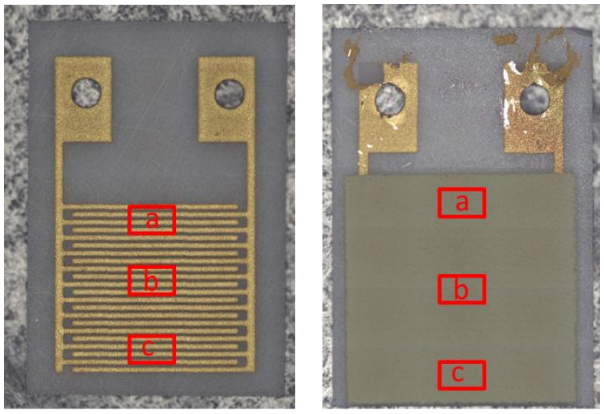

(a) Au paste (b) Sensor element

Fig.3.9 Structural observation of (a) Au paste and (b) film thickness by laser microscopy.

Table 3.5 Average film thickness of the Au paste.

Au paste	Thickness (μm)	Average thickness (μm)	Interval (μm)	Average interval (μm)
a	7.33	6.8	73.57	72.3
b	6.60		73.85	
c	6.43		69.47	

Table 3.6 Average film thickness of the sensor elements.

Sample	Average film thickness(μm)
neat-SnO_2	37.7
1 mol% WO_3-SnO_2-loading	35.5
3 mol% WO_3-SnO_2-loading	36.2
5 mol% WO_3-SnO_2-loading	33.7
1 mol% WO_3-SnO_2-mixing	33.5
3 mol% WO_3-SnO_2-mixing	42.8
5 mol% WO_3-SnO_2-mixing	40.1

3.3 Summary

This chapter firstly studies how calcination under wet oxygen atmosphere affects the growth of SnO_2 nanocrystals, the crystal growth of SnO_2 particles was promoted by introducing water vapor. According to the results of XRD patterns, the peak of WO_3 was detected in the samples with 3 mol% and 5 mol% additions and it was found that the peaks of SnO_2 were shifted toward a small angle with increasing loading amount, indicating that W was doped into the SnO_2 lattice. No relationship between the amount of WO_3 added and the particle size was found. According to the results of nitrogen adsorption–desorption measurement, all samples exhibited typical features of mesoporous structures. The pore volume and average pore diameter increased slightly with the increase of WO_3 content. Subsequently, combining the results of FE-SEM and EDS, the lamellar-structured WO_3 particles in loading group show a fine distribution among SnO_2 particles compared to the mixing group, which may be an important factor affecting the sensor properties. Finally, the film thickness of the sensing layer was measured by laser microscope, and it can be expected that a film thickness of 30-40 μm will facilitate gas diffusion and may have a good response.

4. Characterization of sensing properties

4.1 Introduction

In order to investigate the effect of SnO_2-based materials using WO_3 as the receptor on the electrical characteristics of the sensor, different WO_3 amount of WO_3-loaded SnO_2 as well as WO_3-mixed SnO_2 powders evaluated in Chapter 3 were measured and the characteristics of the sensor were evaluated at an operating temperature range of 200°C-350°C after pretreatment at 480°C for 3h. First, the response characteristics of the sensor were evaluated for the basic gases (gas combustion without intermediate products) H_2 and CO. Then, the response characteristics of simple alcohols (ethanol) and ketones (acetone) were evaluated to study the effect of gases with different reaction pathways on the gas response. Based on the obtained results, the relationship between the sensor response characteristics and the acidic oxide (WO_3) as a receptor was verified.

4.2 Measurement of electrical resistance value under air atmosphere

In this section, resistance values in air were measured using neat-SnO_2, 1 mol%, 3 mol% and 5 mol% WO_3-SnO_2 both loading group and mixing group. Figure 4.1 shows the operating temperature dependence of the electrical resistance value in air. The resistance value measurement starts from high temperature of 350°C to low temperature, it can be clearly seen from the figure that as the temperature decreases, the electrical resistance of each device increases significantly. From the SEM and SEM-EDS results, the reason for the higher electrical resistance exhibited by the 3 mol% and 5 mol% both loading group mixing group may be due to the addition of WO_3, low dispersion of W and the uneven pore size of the sensing layer.

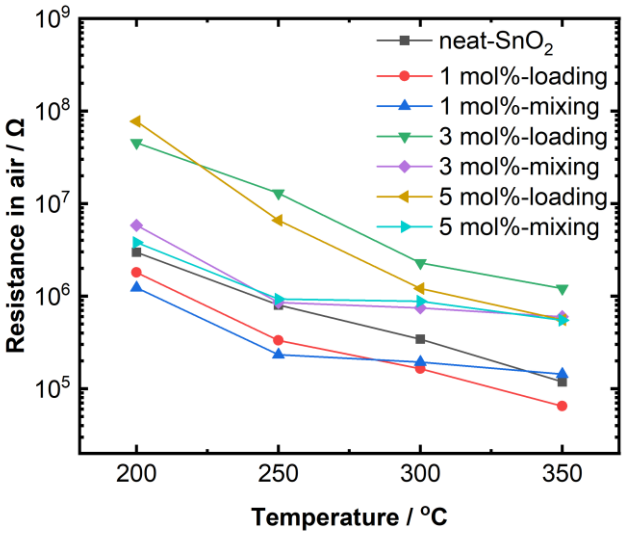

Fig.4.1 The operating temperature dependence of the electrical resistance value in air.

Meanwhile, for 1 mol% WO_3-SnO_2 both loading and mixing, the electrical

resistance is lower than that of neat-SnO_2 at almost each temperature, and some papers gave the following explanations. Even if the depletion layers are formed on the surfaces of SnO_2 and WO_3, some of the transferred electrons in SnO_2 still remain in the conduction band of SnO_2, leading to the increased electron concentration in SnO_2 and thus a decrease in the resistance value [52]. In addition, almost of W was doped into the lattice of SnO_2 in case of the 1 mol% loading and mixing, and it decreases the electrical resistance by W^{6+} substitution with Sn^{4+} site.

4.3 Sensor Response to different gases at different temperatures

4.3.1 H_2 sensing property

Figure 4.2 and 4.3 show the response curve of the sensor to H_2 for WO_3-SnO_2 both loading group and mixing group at the operating temperature range at 200°C to 350°C. After the pretreatment of the sensor, the temperature was lowered to each operating temperature, and after being maintained sufficiently until the resistance value in the air atmosphere became stable, H_2 with a predetermined concentration of 200 ppm was introduced. The operating temperature dependence of the sensor sensitivity is summarized in Figure 4.4.

From Figure 4.2 and 4.3, it can be seen that the time required for the electric resistance of each component to stabilize at different operating temperatures is different, which is caused by the different time required for H_2O to be adsorbed on the surface. It is also evident that the time required for stabilization in H_2/air increases as the operating temperature decreases. This suggests that H_2O is likely to be desorbed when measured at high temperatures, whereas at low temperatures, the hydroxyl may be adsorbed and difficult to desorb.

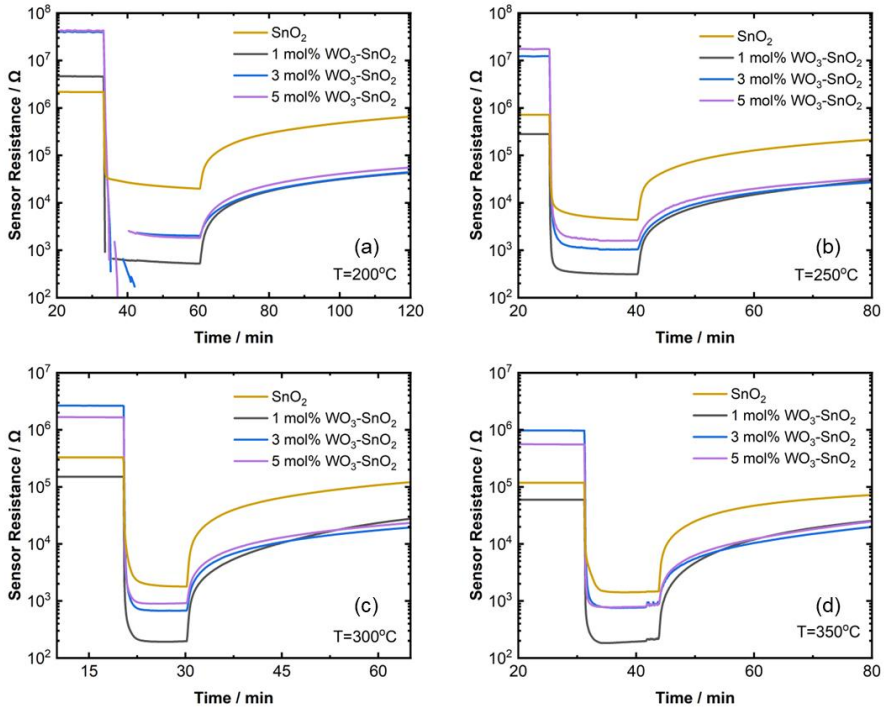

Fig.4.2 The response curve of the sensor to H_2 for WO_3-loaded SnO_2 (a) 200°C, (b) 250°C, (c) 300°C and (d) 350°C.

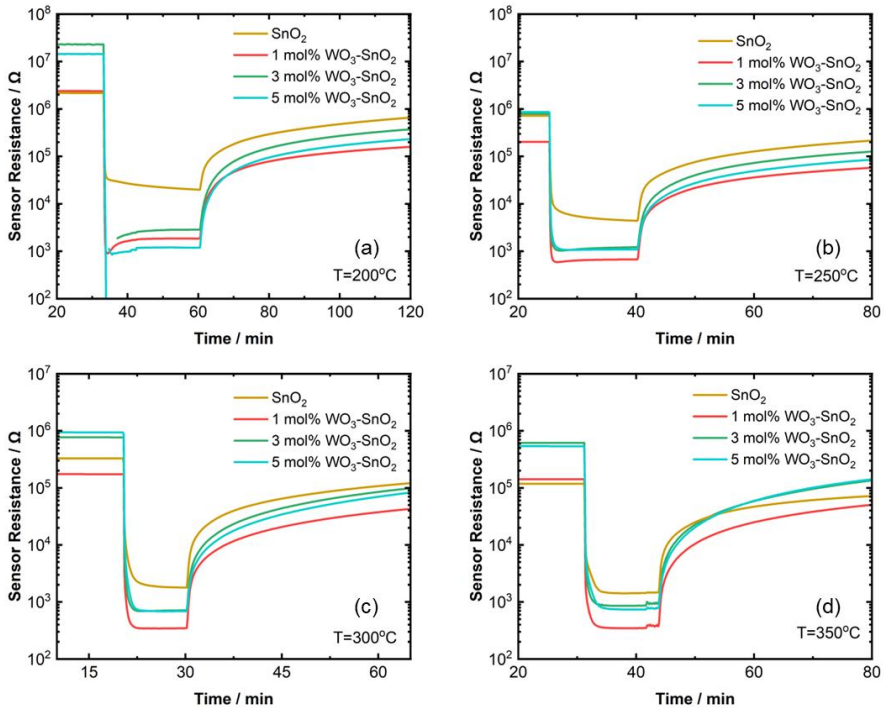

Fig.4.3 The response curve of the sensor to H_2 for WO_3-mixed SnO_2 (a) 200°C, (b) 250°C, (c) 300°C and (d) 350°C.

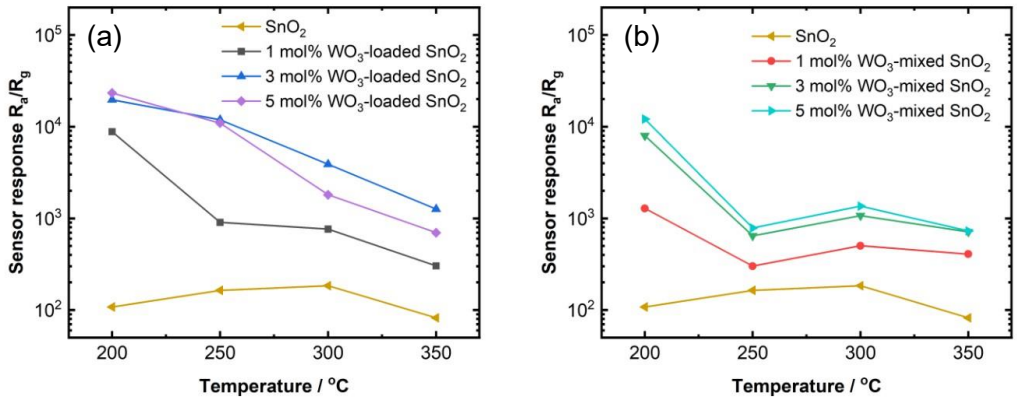

Fig.4.4 The operating temperature dependence of the sensor sensitivity to 20ppmH_2 of (a) WO_3-loaded SnO_2 and (b) WO_3-mixed SnO_2.

As for the loading group and the mixing group, for the target gas H_2, no matter the addition amount of WO_3, the sensor response was much higher than that of neat-SnO_2, and significantly reduced the operating temperature. At 200°C, WO_3-loaded SnO_2 exhibits an ultra-high response to 200ppm H_2, and 3mol% and 5 mol% WO_3-loaded SnO_2 show the highest response, which is 181 and 215 times of the neat SnO_2, respectively.

4.3.2 CO sensing property

The sensor operating temperature of 200ppm CO was also evaluated at 200, 250, 300, and 350°C. Figure 4.5 shows the operating temperature dependence of the sensor sensitivity to CO. It can be seen that the operating temperature dependence of the sensor sensitivity shows a similar behavior for the same concentration of H_2 and CO, such as a significantly lower operating temperature. Similarly, 3 mol% and 5 mol% WO_3-loaded SnO_2 show the highest sensor response. However, the sensitivity to CO is higher than that of H_2, which may be caused by the high oxidation property to CO by WO_3.

The mechanism of the reaction between carbon monoxide (CO) and WO_3-loaded SnO_2 is thought to forms a chemical reaction that is similar to the reaction of CO with neat SnO_2. It is also believed that WO_3-SnO_2 is known to exhibit higher stability towards CO sensing as compare to neat SnO_2 due to the unique electronic structure of WO_3.

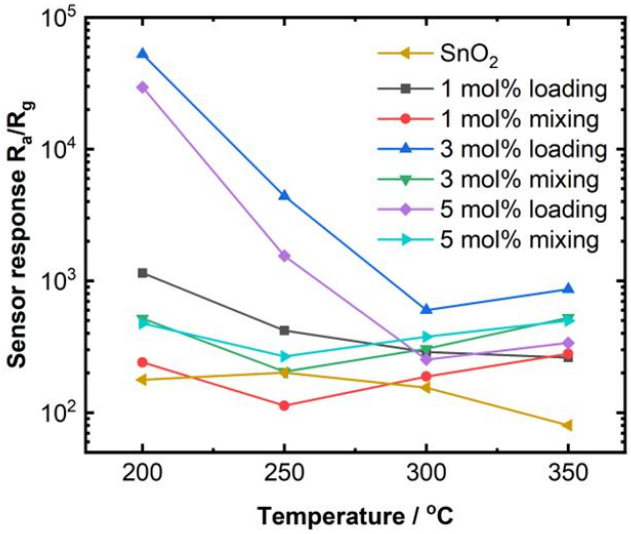

Fig.4.5 The operating temperature dependence of the sensor sensitivity to CO.

4.3.3 Ethanol sensing property

In this section, the ethanol sensing properties of SnO_2, WO_3-loaded SnO_2, and WO_3-mixed SnO_2 under dry atmosphere were verified. Figure 4.6 shows the operating temperature dependence of the sensor sensitivity to ethanol of WO_3-SnO_2 both (a) loading group and (b) mixing group. As shown in the figure, the sensitivity to 20 ppm ethanol tends to be high response at lower temperatures and insensitivity at higher temperatures under the addition of WO_3. However, the sensitivity of neat SnO_2 tends to increase at lower temperatures, but the sensitivity in the presence of WO_3 is higher than that of neat-SnO_2 in any temperature range. The optimum operating temperature for loading group and mixing group is each 250°C and 200°C, respectively. The 3 mol% WO_3-SnO_2 at 250°C shows the highest response, which is 14.4 times that of the neat-SnO_2. This can be explained according to the previous data. For neat-SnO_2, ethanol gas reached 90% conversion at 300ºC. The primary product from ethanol gas was CH_3CHO, which was converted to CO_2 and CO increasingly at higher temperature. On the other hand, for WO_3-loaded SnO_2, the addition of WO_3 can be considered changed the reaction path, the ethanol gas undergoes dehydration at elevated temperature and reached more than 90% conversion at about 250ºC, with the main product being C_2H_4 and the conversion of CO_2 continuing to gradually increase at higher temperatures [44]. Thus, it is concluded that the decrease in operating temperature is dominated by W^{6+}.

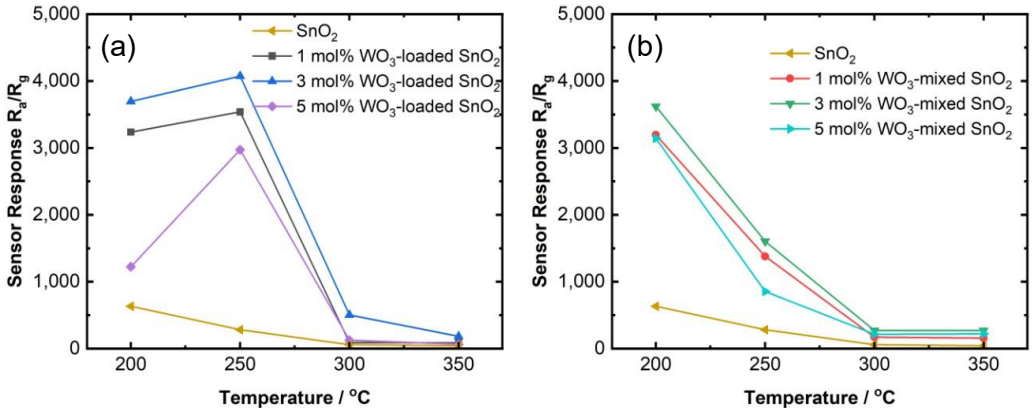

Fig.4.6 The operating temperature dependence of the sensor sensitivity to ethanol of WO_3-SnO_2 both (a) loading group and (b) mixing group.

Figure 4.7 shows the corresponding response at ethanol concentrations ranging from 1–40 ppm at the operating temperature 250°C. It can be seen from the figure that the sensor response increases linearly with the increase of ethanol concentration. Even at a low concentration of 1 ppm ethanol, the responses of the sensors fabricated by neat SnO_2 NPs, 1%, 3% and 5% WO_3–loaded SnO_2 NPs are 12.3, 18.5, 125.1, and 124.7, respectively. It can be shown that the addition of WO_3 has a better response to lower concentrations of ethanol.

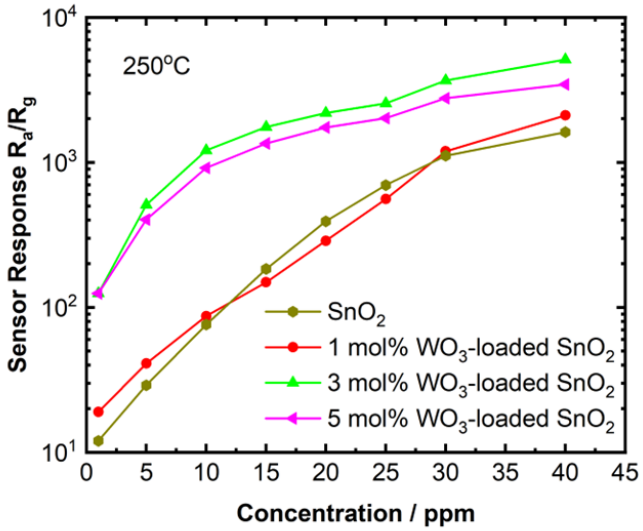

Fig.4.7 The corresponding response values at ethanol concentrations ranging from 1–40 ppm.

4.3.4 Acetone sensing property

Figure 4.8 shows the operating temperature dependence of the sensor sensitivity

to ethanol of WO_3-SnO_2 both (a) loading group and (b) mixing group. As a result, for 20ppm acetone, it can be concluded that both for loading group and mixing group, it shows higher response than the neat SnO_2, the loading group shows a higher response than the mixing group. And as the temperature decreases, the response of both groups to acetone increases, for the loading group, the optimal operating temperature is 250°C, on the other hand, for the mixing group, the optimal operating temperature is 200°C. Moreover, the 3 mol% WO_3-loaded SnO_2 shows the highest response at the optimum operating temperature 250°C, which is 12.9 times that of the neat-SnO_2.

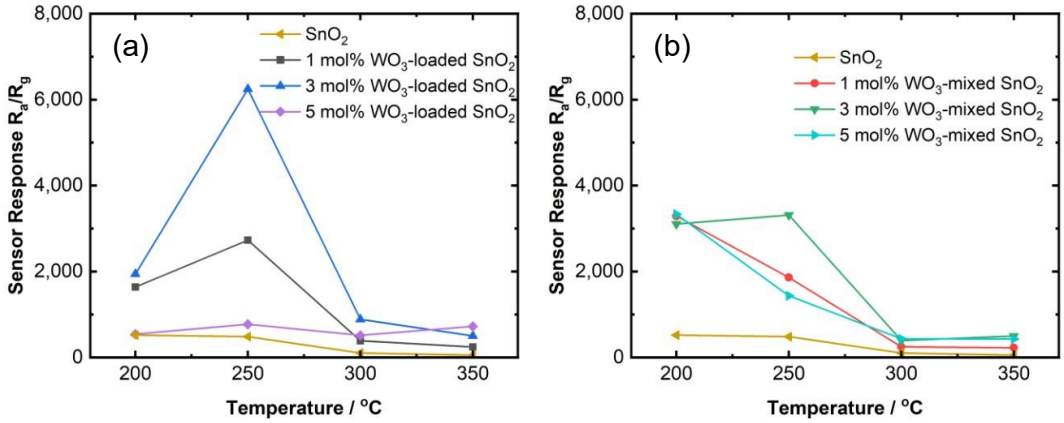

Fig.4.8 The operating temperature dependence of the sensor sensitivity to ethanol of WO_3-SnO_2 both (a) loading group and (b) mixing group.

4.4 Property differences between loading group and mixing group

Section 4.3 shows the response properties of neat SnO_2, 1, 3 and 5 mol% WO_3-SnO_2 each loading and mixing group materials for different target gases. Figure 4.9 shows the temperature dependence of the sensor sensitivity to 20ppm ethanol and acetone. As for ethanol and acetone, both the WO_3 loaded and mixed SnO_2 show higher response than neat-SnO_2 at each temperature. In addition, the shift of the optimum operating temperature by WO_3-loaded SnO_2 at 250ºC may be due to the change in reaction path. In case of ethanol, according to the previous report, ethylene was produced via the ethanol combustion on the acidic surface, and it needs high temperature to produce CO_2 and H_2O [44]. On the other hand, the reaction path of ethanol combustion on the SnO_2 and WO_3-mixed SnO_2 were almost similar, because WO_3 is present as large and low-dispersity particle through the combination with the XRD and SEM results. Here, the sensor response using WO_3-mixed SnO_2 is larger than neat SnO_2, but the curve trends are similar, which suggests that the reaction paths of SnO_2 and WO_3-mixed SnO_2 seem to be the same, and the enhanced response is probably caused by difference in utility factor of both, such as pore size and distribution of the sensing layer. Similarly, a similar phenomenon to acetone was observed for both WO_3 loaded and mixed SnO_2 as for ethanol, implying that the reaction path may be the same as that of ethanol, but the intermediate products of the acetone reaction cannot be determined

at present, except that the loading of WO_3 similarly changes the reaction path, which requires further research.

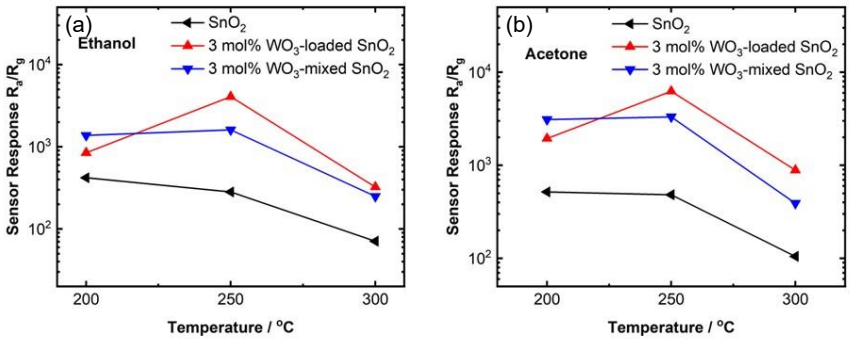

Fig.4.9 The temperature dependence of the sensor sensitivity to 20ppm ethanol and acetone.

Figure.4.10 shows the dependence of the WO_3 content amount dependence of the sensor response to 20ppm ethanol and acetone at 250ºC and 200ºC. It can be clearly seen that the 3 mol% WO_3-loaded SnO_2 shows the highest response at 250ºC, and increasing the loading amount reduces the response probably because of the aggregation of WO_3. In contrary, in case of ethanol, the sensor response at 200ºC using WO_3-loaded SnO_2 is lower than that of WO_3-mixed SnO_2 when the WO_3 content above 3mol%. It indicates that surface combustion activity of SnO_2 is reduced by WO_3 loading with highly dispersion, because site for gas detection is reduced by highly dispersed WO_3 particles.

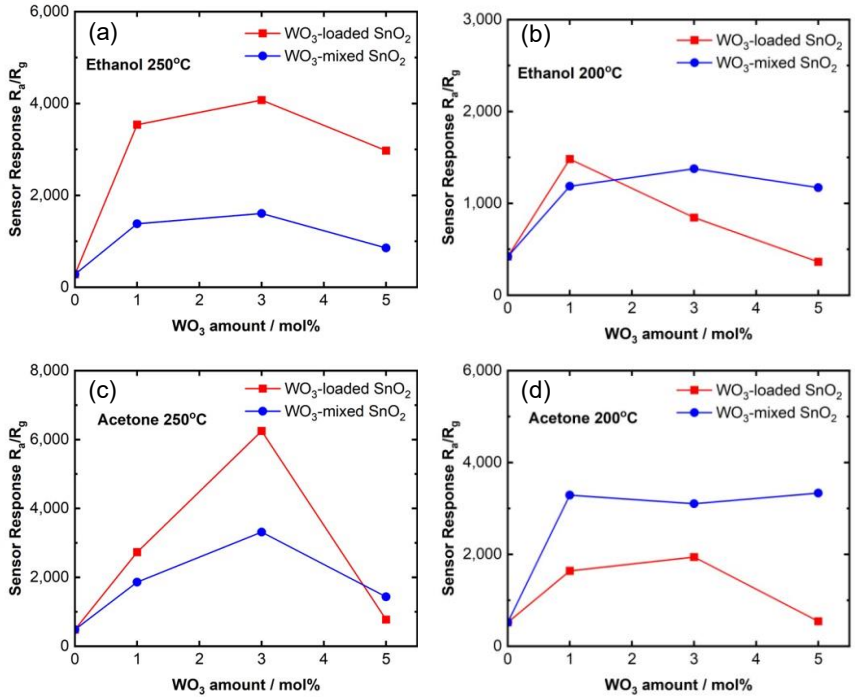

Fig.4.10 Dependence of the WO_3 content amount to 20 ppm ethanol and acetone at 250ºC and 200ºC.

4.5 Summary

In this chapter, the electrical and sensor response characteristics of the sensors were evaluated using different loading amount of WO_3-SnO_2 calcined at 480°C. Among them, 3 mol% and 5 mol% of both the loading group and mixing group showed higher resistance values in air. In addition, the sensors of both groups showed high sensitivity for both H_2 and CO compared to neat-SnO_2 and significantly lower operating temperatures. On the other hand, for ethanol and acetone, for the loading group, the 3 mol% addition of WO_3 showed a higher response at 250°C, while the mixing group showed results that, although it was less sensitive than the loading group, the mechanical mixing reduced the operating temperature, which showed a better response at 200°C. This phenomenon is consistent with the curve of neat SnO_2, but the increase in sensitivity may be due to the utility factor. The different curves exhibited by the loading groups may be due to the change of the reaction pathway dominated by the addition of WO_3.It's considered that utility factor only enhances the sensor response of WO_3-mixed SnO_2. While combining that utility factor and surface combustion ability enhances and shifts the sensor response and optimal operating temperature, respectively. However, the intermediate products of combustion of acetone need to be further investigated. Moreover, due to the few target gases tested so far, it is difficult to show that the loading of WO_3 can be selectivity detect acetone, although 3 mol% WO_3-SnO_2 shows the highest response. From the above results, it is shown that WO_3 as receptor strongly influences the response characteristics of the sensors and this acidic oxide addition is an effective factor in the material design.

5. Conclusions and Future Research

5.1 Conclusions

Metal oxide semiconductor (MOS) gas sensors were proposed by Seiyama et al., and Taguchi et al., in 1962, and many studies have been reported. The SnO_2-based semiconductor gas sensors can be used to detect low concentrations of combustible gases such as volatile organic compound (VOC) gases and features high sensitivity and long-term stability. The basic mechanism of the gas sensor is that the surface of the semiconductor material reacts with an oxidizing or reducing gas, resulting in a change in the electrical resistance of the material. So far, our laboratory has proposed three key factors for fabricating highly sensitive gas sensors. This thesis mainly focuses on the receptor function. Previously, Jinkawa et al., has reported the surface catalytic property of SnO_2 sensors modified with acidic or basic oxides, the reaction path in the oxidation reaction of ethanol can be controlled. For example, oxide has acidic surface, ethanol combustion proceeds via production of ethylene. In contrary, acetaldehyde is produced by byproducts of ethanol combustion on basic surface. The particles size and its dispersity are strongly influenced by compositing method of receptor oxide and should affect the receptor function. However, these receptor-related theories are not established well. Thus, this study focused on WO_3 as an acidic receptor and the receptor effect based on two WO_3 compositing methods on its sensing properties was investigated.

In Chapter 1, we explained gas sensors and described the detection mechanism of SnO_2-based semiconductor gas sensors. We also explained three key factors for fabricating highly sensitive gas sensors: receptor function, transducer function, and utility factors that our laboratory has proposed so far. Some descriptions are also provided for the receptor function. Finally, the motivations of this study are presented.

In Chapter 2, we illustrated the two methods for the synthesis of SnO_2 and WO_3-SnO_2 and the method for evaluating the obtained materials in this study. In addition, the fabrication of the sensor element and the method of measuring the resistance value are explained.

In Chapter 3, we first investigated the effect of calcination of SnO_2 in a wet oxygen atmosphere on crystalline growth. And then according the XRD pattern, the peak of WO_3 was detected in the samples with 3 mol% and 5 mol% additions and it was found that the peaks were shifted by the addition of WO_3, indicating that W was doped into the SnO_2 lattice. Subsequently, combining the results of FE-SEM and EDS, the lamellar-structured WO_3 particles in loading group show a fine distribution among SnO_2, this can give some reasonable explanations for the test results obtained in Chapter 4. Finally, the film thickness of the sensing layer was measured by laser microscope, the results show that the sensing layer thickness was similar for various materials.

In Chapter 4, we evaluated the electrical and sensor response characteristics of the sensors using different WO_3 content amount of WO_3-SnO_2. The addition of WO_3 of 3 mol% and 5 mol% in both the loading group and mixing group showed higher resistance values in air. For H_2 and CO, the sensors of both groups showed high sensitivity and significantly lower operating temperatures. On the other hand, for ethanol and acetone, 3 mol% addition of WO_3 for loading group shows the highest response at 250°C, while the mixing group shows the lower operating temperature. In

the low-temperature region, WO_3-mixed SnO_2 exhibits the same trend as neat SnO_2, but with an increase in sensitivity, which suggests that the reaction path is unchanged and the increase in sensor response is caused by the utility factor. In case of ethanol, for WO_3-loaded SnO_2, the optimal operating temperature shifted to 250°C, this result may be due to the change of reaction path that ethylene was produced via the ethanol combustion on the acidic surface. Thus, formation of fine and highly dispersed WO_3 on SnO_2 surface provide the effect of acidity on the particles surface. Also, increasing the WO_3 amount reduces the sensor response regardless of loading method that probably caused by the aggregation of WO_3. Therefore, dispersion of the WO_3 nanoparticles enhance the sensor response to ethanol at high temperature by tuning the reaction path. This is useful way to design the sensor properties such as sensor response and optimized operating temperature. From the above results, it is shown that WO_3 as a receptor strongly influences the response properties and this acidic oxide addition is an effective factor in the material design.

5.2 Future Research

The present study shows that the addition of acidic oxide WO_3 as receptor to the SnO_2-based sensor can significantly reduce the operating temperature as well as improve the sensor response. Among them, 3 mol% is the optimal addition amount. This study contributes to a better understanding of the sensing properties of gas sensors using acidic oxide (WO_3) as receptor and the basis for the effects of additives. In order to further clarify the surface process of gas sensing, explore the catalytic mechanism of additives, and promote the sensing performance and especially selectivity of SnO_2-based gas sensor, the following aspects are put forward on the basis of present thesis for future research.

1.Using TPD/TPR to evaluate the oxygen and volatile organic compound (VOC) gases adsorption/desorption performance of the sensor materials, and explore the catalytic property of WO_3 as receptor through intermediate products and reaction pathways.

2. To further improve the gas selectivity, especially among VOC gases, was attempted by introducing MEMS sensor and pulse-driven modes [62-64]. Traditional semiconductor gas sensors have large component size and power consumption, so MEMS was developed to solve this problem. The purpose of using this pulse-driven mode is to improve selectivity and sensitivity by exploiting the difference in resistance change when driving with temperature modulation according to the gas type. It is proposed that VOC gases adsorb on the particle surface during the low-temperature heater-off phase and the adsorbed gases combust during the high-temperature heater-on phase. This gas detection model allows for improvements in gas selectivity based on the gas adsorption and catalytic combustion properties on the SnO_2 surface, however this application also has the potential to change the reaction path.

3. Based on WO_3-loaded SnO_2, it is possible to modify the receptor with a cation of the same or similar valence as the W element ($WO_3+\alpha$) such as Mo^{6+} or V^{5+}. However, such reported studies are incomplete, but it is speculated that this method can be used

to obtain improved gas selectivity by enhancing the surface acidity to further change the reaction path.

4. It has been known that receptor function displayed an important influence on gas selectivity. Therefore, it is vital to select appropriate foreign receptors to design highly selective gas sensors. So far, we proposed receptor function using single oxide or noble metal. However, the effect of double receptors has not been investigated in detail. Noble metals (Au, Pd, Pt) can provide strong electron sensitization, so using the current acidic metal oxide (WO_3) and noble metal as a second receptor may be one of the important factors to achieve high selectivity.

Reference

[1] 株式会社石油産業新聞社「歴史を綴ったエピソード」http://www.sekiyusangyo.co.jp/news/rekishi/rekisshi01.html

[2] Yamazoe, N. (2005). *Sens. Actuators B Chem.*, 108(1-2), 2-14.

[3] Kohl, D. (2001). *J. Phys. D: Appl. Phys.*, 34(19), R125.

[4] Neri, G. (2015). *Chemosensors*, 3(1), 1-20.

[5] Göpel, W., & Schierbaum, K. D. (1995). *Sens. Actuators B Chem.*, 26(1-3), 1-12.

[6] Li, Z., Li, H., Wu, Z., Wang, M., Luo, J., Torun, H., ... & Fu, Y. (2019). *Mater. Horizons*, 6(3), 470-506.

[7] Timmer, B., Olthuis, W., & Van Den Berg, A. (2005). *Sens. Actuators B Chem.*, 107(2), 666-677.

[8] Seiyama, T., Kato, A., Fujiishi, K., & Nagatani, M. (1962). *Anal. Chem.*, 34(11), 1502-1503.

[9] Taguchi, N. (1962). Published patent application in Japan. S37-47677, October.

[10] フィガロ技研株式会社，フィガロの歩み，https://www.figaro.co.jp/company/history.html

[11] Shaver, P. J. (1967). *Appl. Phys. Lett.*, 11(8), 255-257.

[12] Tomer, V. K., Singh, K., Kaur, H., Shorie, M., & Sabherwal, P. (2017). *Sens. Actuators B Chem.*, 253, 703-713.

[13] Amann, A., de Lacy Costello, B., Miekisch, W., Schubert, J., Buszewski, B., Pleil, J., ... & Risby, T. (2014). *J. Breath Res.*, 8(3), 034001.

[14] Phillips, M., Herrera, J., Krishnan, S., Zain, M., Greenberg, J., & Cataneo, R. N. (1999). *J. Chromatogr. B Biomed. Appl.*, 729(1-2), 75-88.

[15] Grabowska-Polanowska, B., Faber, J., Skowron, M., Miarka, P., Pietrzycka, A., Śliwka, I., & Amann, A. (2013). *J. Chromatogr. A*, 1301, 179-189.

[16] Ogimoto, Y., Selyanchyn, R., Takahara, N., Wakamatsu, S., & Lee, S. W. (2015). *Sens. Actuators B Chem.*, 215, 428-436.

[17] Kim, N. H., Choi, S. J., Yang, D. J., Bae, J., Park, J., & Kim, I. D. (2014). *Sens. Actuators B Chem.*, 193, 574-581.

[18] Shin, J., Choi, S. J., Lee, I., Youn, D. Y., Park, C. O., Lee, J. H., ... & Kim, I. D. (2013). *Adv. Funct. Mater.*, 23(19), 2357-2367.

[19] Lin, Y., Deng, P., Nie, Y., Hu, Y., Xing, L., Zhang, Y., & Xue, X. (2014). *Nanoscale*, 6(9), 4604-4610.

[20] Adiguzel, Y., & Kulah, H. (2015). *Biosens. Bioelectron.*, 65, 121-138.

[21] 清山哲郎. 化学センサ実用便覧[J]. フジ・テクノシステム, 1986: 222-225.

[22] 清山哲郎、塩河二朗、鈴木周一、笛木和雄、化学センサー、講談社(1982 年 3 月)

[23] Ogawa, H., Nishikawa, M., & Abe, A. (1982). *J. Appl. Phys.*, 53(6), 4448-4455.
[24] Korotcenkov, G. (2005). *Sens. Actuators B Chem.*, 107(1), 209-232.
[25] 末松昂一、博士論文（九州大学）(2012).
[26] Yamazoe, N., Fuchigami, J., Kishikawa, M., & Seiyama, T. (1979). *Surf. Sci.*, 86, 335-344.
[27] Y. Mizokawa and S. Nakamura, *Japan. J. Appl. Phys*. 46 (1977) 580.
[28] Thornton, E. W., & Harrison, P. G. (1975). *J. Chem. Soc., Faraday Trans. 1*, 71, 461-472.
[29] 山添昇, 電子技術, 25, 44(1983).
[30] Yamazoe, N., Kurokawa, Y., & Seiyama, T. (1983). *Sens. Actuators*, 4, 283-289.
[31] Noboru Ichinose, Yuji Yokomizo, Masaki Katsura, Institute of Electrical Engineers of Japan, Electronic Equipment Study Group Materials EDD-75-53 (1975).
[32] Meng, X., Bi, M., Xiao, Q., & Gao, W. (2022). Int. J. Hydrog. Energy, 47(5), 3157-3169.
[33] Yamazoe, N., & Shimanoe, K. (2008). *Sens. Actuators B Chem.*, 128(2), 566-573.
[34] Xu, C., Tamaki, J., Miura, N., & Yamazoe, N. (1991). *Sens. Actuators B Chem.*, 3(2), 147-155.
[35] C. N. Xu, J. Tamaki, N. Miura, N. Yamazoe, Chem. Lett., 1990(3), 441 (1990).
[36] Yamazoe, N., & Shimanoe, K. (2008). *J. Electrochem. Soc.*, 155(4), J85.
[37] Yamazoe, N., & Shimanoe, K. (2009). *J. Sens.*, 2009.
[38] Yamazoe, N., & Shimanoe, K. (2009). *Sens. Actuators B Chem.*, 138(1), 100-107.
[39] Yamazoe, N., & Shimanoe, K. (2009). *Thin Solid Films*, 517(22), 6148-6155.
[40] Matsunaga, N., Sakai, G., Shimanoe, K., & Yamazoe, N. (2002). *Sens. Actuators B Chem.*, 83(1-3), 216-221.
[41] Sakai, G., Matsunaga, N., Shimanoe, K., & Yamazoe, N. (2001). *Sens. Actuators B Chem.*, 80(2), 125-131.
[42] Matsunaga, N., Sakai, G., Shimanoe, K., & Yamazoe, N. (2003). *Sens. Actuators B Chem.*, 96(1-2), 226-233.
[43] 田部 浩三 , 清山 哲郎 , 笛木 和雄 編 , 金属酸化物と複合酸化物 調製・物性・構造・触媒作用・無機材質との関連 , 講談サイエンティフィック , 407-414 (1978)."
[44] Jinkawa, T., Sakai, G., Tamaki, J., Miura, N., & Yamazoe, N. (2000). *J Mol Catal A Chem.*, 155(1-2), 193-200.
[45] Iwamoto, M., Yoda, Y., Yamazoe, N., & Seiyama, T. (1978). *J. Phys. Chem.*, 82(24), 2564-2570.
[46] Iwamoto, M., Maruyama, K., Yamazoe, N., & Seiyama, T. (1977). *J. Phys. Chem.*, 81(7), 622-629.
[47] Ling, Z., & Leach, C. (2004). *Sens. Actuators B Chem.*, 102(1), 102-106.
[48] Iwamoto, M., Yoda, Y., Yamazoe, N., & Seiyama, T. (1978). *Bull. Chem. Soc. Jpn.*, 51(10), 2765-2770.
[49] Yin, M., Yao, Y., Fan, H., & Liu, S. (2018). *J. Alloys Compd.*, 736, 322-331.
[50] Zhu, Y., Wang, H., Liu, J., Yin, M., Yu, L., Zhou, J., ... & Qiao, F. (2019). *J. Alloys Compd.*, 782, 789-795.
[51] Tomer, V. K., Devi, S., Malik, R., Nehra, S. P., & Duhan, S. (2016). *Sens. Actuators*

B Chem., 229, 321-330.
[52] Van Toan, N., Hung, C. M., Van Duy, N., Hoa, N. D., Le, D. T. T., & Van Hieu, N. (2017). *Mater. Sci. Eng. B*, 224, 163-170.
[53] Zhang, J., Zhang, L., Leng, D., Ma, F., Zhang, Z., Zhang, Y., ... & Lu, H. (2020). *Sens. Actuators B Chem.*, 306, 127575.
[54] Li, H. Y., Cai, Z. X., Ding, J. C., & Guo, X. (2015). *Sens. Actuators B Chem.*, 220, 398-405.
[55] Zhang, Z., Yin, C., Yang, L., Jia, W., Zhou, J., Xu, H., & Cao, D. (2017). *Ceram. Int.*, 43(9), 6693-6699.
[56] Hoa, T. T. N., Le, D. T. T., Van Toan, N., Van Duy, N., Hung, C. M., Van Hieu, N., & Hoa, N. D. (2021). *Mater. Today Commun.*, 26, 102094.
[57] Shao, S., Chen, X., Chen, Y., Lai, M., & Che, L. (2019). *Applied Surf. Sci.*, 473, 902-911.
[58] 花中秋. (2014). (Doctoral dissertation, 九州大学).
[59] 江藤守總. (1998). 機器分析の基礎.
[60] Shimanoe, K., Nishiyama, A., Yuasa, M., Kida, T., & Yamazoe, N. (2009). *Procedia Chem.*, 1(1), 212-215.
[61] Kida, T., Fujiyama, S., Suematsu, K., Yuasa, M., & Shimanoe, K. (2013). *J. Phys. Chem. C*, 117(34), 17574-17582.
[62] Suematsu, K., Oyama, T., Mizukami, W., Hiroyama, Y., Watanabe, K., & Shimanoe, K. (2020). *ACS Appl. Electron. Mater.*, 2(9), 2913-2920.
[63] Suematsu, K., Harano, W., Yamasaki, S., Watanabe, K., & Shimanoe, K. (2020). *ACS Appl. Electron. Mater.*, 2(12), 4122-4126.
[64] Suematsu, K., Hiroyama, Y., Harano, W., Mizukami, W., Watanabe, K., & Shimanoe, K. (2020). *ACS sensors*, 5(11), 3449-3456.

Acknowledgements

First of all, I would like to give my heartfelt thanks to all the people who have ever helped me in this thesis.

My sincere and hearty thanks and appreciations go firstly to my supervisor, Prof. Kengo Shimanoe, whose suggestions and encouragement have given me much insight into my research. It has been a great privilege and joy to study under his guidance and supervision. Furthermore, it is my honor to benefit from his personality and diligence, which I will treasure my whole life.

Second, I would like to express my heartfelt gratitude to Prof. Ken Watanabe and Dr. Koichi Suematsu whose gave me a lot of academic and life guidance.

I am also extremely grateful to all former and present members of our research group: Mrs. Yoshida, Mrs. Shinagawa, Mrs. Hoshino, Dr. Okuda, Mr. He, Mr. Takeno, Ms. Yang, Mr. Kamitani, Mr. Tashiro, Mr. Mikata, Mr. Ueda, Mr. Yanagawa, Mr. Fukuno, Mr. Kunisaki, Mr. Naito, Mr. Kobayashi and Mr. Aoki who have kindly provided me assistance and companionship.

Finally, many thanks go to my family for their financial support, unfailing love and unwavering encouragement during my master's course in Japan. I would also like to thank my like-minded friends for their spiritual support in my life.